Development of tools and methods for KATRIN DPS2-F test experiments

Marcel Christian Robert Zoll

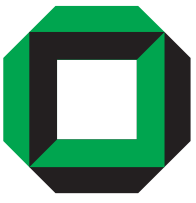

Institut für Experimentelle Kernphysik
Universität Karlsruhe (TH)

Development of tools and methods for KATRIN DPS2-F test experiments

Diploma Thesis

presented
by

Marcel Christian Robert Zoll

Institut für Experimentelle Kernphysik
Universität Karlsruhe (TH)
August 2009

Contents

1. Introduction

During the elaboration of this thesis particle physics had a presence in the public press seldom seen before. People were discussing the ifs and whys of physics and some even tried to freshen up their knowlegde on developments in physics in recent years. Special interest was paid to the LHC and its search for the Higgs particle that was hypothesized in 1964 to solve major problems in particle physics such as the generation of masses. Should it in fact be found it would validate and complete the present most common interpretation of particle physics, the standard model (SM).

The standard model interprets the universe and its inner phenomena by its smallest essential building blocks, the elementary particles, and their interactions. The SM contains quarks (building up e.g. protons and neutrons which in turn build up atom nuclei) and leptons (e.g. electrons that determine electrical properties); the particles are divided in three generations stacking nicely in an increasing mass order. Finally bosons (e.g. photons, massless electromagnetic particles) mediate interactions between those particles.

The standard model is very popular and preferred right because its simple formulation

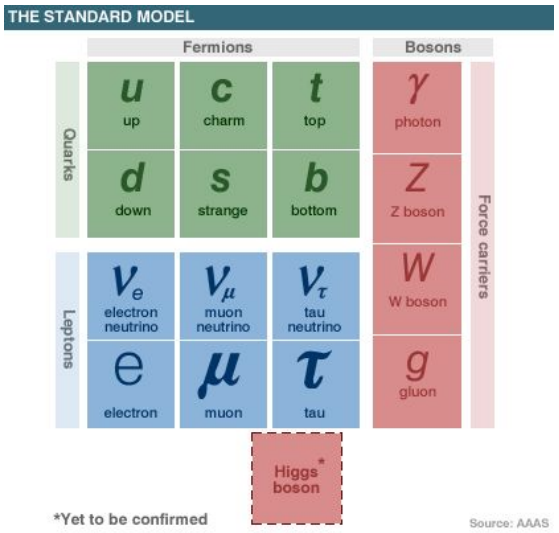

Figure 1.1: **The standard model of particle physics**

bares an inner beauty. But while LHC investigates the high energy regime to complete this model some key links in the low energy regime are still missing or are incomplete. For example the neutrino, which is the neutral partner in weak force interactions, is still a particle of uncertainty. While all other particles' rest masses were very narrowly

pinpointed down during the last years, no such feat could be accomplished for the neutrino. The cause of this should be stated soon, but not before the character of the neutrino is enlightened in a historical way.

Before 1930 particle physics had problems explaining the kinematics of the radioactive beta-decay: It was known that in the decay process a core based neutron is converted into a proton and an electron which is propelled out of the core. The energy spectrum of the electron as it is discribed by a two body problem was expected to be sharp. The experimental review however revealed a continuous spectrum clearly in contradiction to this.
Wolfgang Pauli presented a solution by adding a hypothetical particle to the reaction

$$\mathrm{n} \rightarrow \mathrm{p} + \mathrm{e}^- + \overline{\nu_\mathrm{e}} \tag{1.1}$$

By doing so the problem is transferred into a three body problem, explaining the continuous spectrum and solving the discrepancy in energy and momentum conservation. However this theoretical particle could not be directly observed at this time.

In 1934 Enrico Fermi's theory of β-decay firmly included this particle without rest mass by the new name "neutrino". The generalization of the β-decay as a reaction mediated by the weak force was later extended to the modern V-A-theory. To comply with this theory the neutrino still had to have zero rest mass. The theoretical framework could also explain why no direct detection of the neutrino had then been possible yet: the calculated cross section for an average neutrino would be so low that it might travel through massive amounts of matter without interaction.

It was not until 1956 that Reines and Cowan succeeded in the direct detection of the neutrino by the inverse β^+-decay reaction:

$$\overline{\nu_\mathrm{e}} + \mathrm{p} \rightarrow \mathrm{n} + \mathrm{e}^+ \tag{1.2}$$

The quite challenging task was to find a specific detection mechanism that is unique only to the rare neutrino related events. Only when both reaction products, the positron and neutron, are identified as related to the same event, the causality to the neutrino would stand. The experiment identified the positron by the coincidental detection of the annihilation photons and the deexcitation photon emitted when the neutron is captured on a cadmium nucleus [Cow56] [Rein56].

The results of later experiments then started to shake the initial assumption of the zero mass neutrino. In fact they preferred a non-zero rest mass to better explain their findings.
The scientific and technological evolution had by then made it possible to push forward deeper into neutrino properties. Better and more sensitive detector devices enabled research into other sectors that could not be investigated before. Also the availability of newer stronger neutrino sources contributed their share, as in high power nuclear

reactors, where the neutrinos are produced as a byproduct in the fission process. Accelerators provide narrow beams of neutrinos for example from pion (π) decays. Also, natural neutrino sources like stars became subjects of research.

All stars, including our sun, gain their immense power by the collection and compression of stellar gases like hydrogen. This itself already generates heat. But at a certain point the density and temperature of the matter becomes so great that atom nuclei begin to fuse. This process is called stellar fusion and is the star's main energy source. In its early stages a star begins to convert protons into neutrons and thereby compose heavier nuclei so that in further chain reactions helium is built up (pp-cycle). The total reaction reads

$$4\mathrm{p} + 2\mathrm{e}^- \rightarrow {}^4\mathrm{He} + 2\nu_\mathrm{e} + \Delta E \tag{1.3}$$

Neutrinos which are created in the dense core of the star can leave this region undisturbed because of their tiny cross-section. Their number and energy can be precisly calculated by equilibrium equations.

The sun constantly bombards earth with an electron-neutrino flux of approximatly $6{\cdot}10^{14}$ per square meter per second. Only one of 10^{12} causes an interaction when passing through the earth [Gru09]. Nevertheless different projects were set up to validate this quantity. In fact, these experiments were able to detect the solar electron neutrino flux. The levels however were always in discrepancy with the calculations.
Stated here is a short list of famous experiments in this field and their findings:

- The experiments Homestake, Gallex/GNO and SAGE used a radiochemical detection method based upon neutrino capture:

  $$^N_Z\mathrm{A} + \nu_\mathrm{e} \rightarrow {}^N_{Z+1}\mathrm{B} + \mathrm{e}^- \tag{1.4}$$

  The change in charge number affects the chemical behavior and allows the extraction of the radioactive daugther nucleus. This method is however only sensitive to electron-neutrinos and could provide no directional information.
  All experiments, though, agree that the measured flux of electron flavored neutrinos is smaller by a factor of 2 to 3 than the predicted value [Lan03], [Ver02], [Dav94], [Ham99].

- (Super)Kamiokande is an experiment that specialized in the detection and tracking of neutrino events. The experiment looked for scattering reactions on electrons

  $$\nu + \mathrm{e}^- \rightarrow \nu' + \mathrm{e}^{-\prime} \tag{1.5}$$

  In principle, this reaction is not limited to neutrinos with electron flavor, but the reaction probability for those events increases over both other flavors by a factor of 7.
  The experiment consists of a huge tank holding $50000\,\mathrm{m}^3$ of pure water. The tank's walls are equipped all over with photomultiplier tubes. Should a charged particle travel within the tank with a velocity greater than the respective speed of light it will emit a cone of Cherenkov light detected by the PMTs. The experiment therefore looks for the appearance of this phenomenon caused by scattered

electrons. Analysis of the Cherenkov light characteristics allows the reconstruction of theinitial neutrino direction. This enabled the experiment to discriminate events not related to the sun.
The results of (Super)Kamiokande stated that only 36% of the expected solar neutrino flux could be observed [Kam03].

- KamLAND used the inverse β-decay reaction of β^+-decay of Reines and Cowan to check the flux of all japanese nuclear reactors. Only 61% of the expected flux was found inside the detector [KL03] [KL04].

The above stated experiments demonstarted that a part of the neutrinos had vanished or that there is a major flaw in the fundamental physics assumptions. A possible explanation for this could be given by the so called neutrino flavor oscillations. The neutrinos do not vanish but convert into a different flavor state as they travel. For example an original solar electron neutrino, while it covered the distance to earth, transferred into a muon neutrino that was not accessible for the experiment.
This theory was first introduced in 1958 by Bruno Pontecorvo, but had to wait until 2001 before the Sudbury Neutrino Observatory (SNO) experiment would present data that could validate its correctness.

The SNO detector was designed as a spherical heavy water (D_2O) tank with photomultipliers that was surrounded by an additional veto tank filled with light water (H_2O). SNO was able to detect three different kinds of reactions simultaneously:

1. elastic neutrino scattering on electrons:

$$\nu + \mathrm{e}^- \rightarrow \nu' + \mathrm{e}^{-\prime} \tag{1.6}$$

   by detecting Cherenkov light, which is sensitive to all three kinds of flavors, but favored for ν_e.

2. charged currents (CC):

$$\nu_\mathrm{e} + \mathrm{D} \overset{\mathrm{W}^\pm}{\rightarrow} \mathrm{p} + \mathrm{p} + \mathrm{e}^- \tag{1.7}$$

   in deuterium results in a breakup of nuclei. This is allowed for the electron type flavor, due to the different energy thresholds for ν_μ and ν_τ. Therefore the CC is exclusively for ν_e.

3. neutral currents (NC):

$$\nu + \mathrm{D} \overset{\mathrm{Z}^0}{\rightarrow} \mathrm{p} + \mathrm{n} + \nu' \tag{1.8}$$

   The neutron is detected upon capture by emitted photon, with the NC being sensitive to all flavors.

By evaluation of the rates of the three different channels SNO confirmed the missing number of solar electron neutrinos, but also found that the total flux over all flavors was in good agreement with the prediction. The flavor transformation of the neutrino

as the origin of the solar ν problem had been proven!

The theory of neutrino oscillation is based upon the assumption that the weak interaction eigenstates are superpositions of different mass eigenstates. This means that every neutrino flavor state, the eigen state in weak processes, is made up of contributions of three mass states, describing the Higgs interaction, and vice versa.

$$\begin{aligned} |\nu_\alpha\rangle &= \sum_i \mathrm{U}^*_{\alpha i} |\nu_i\rangle \\ |\nu_i\rangle &= \sum_i \mathrm{U}_{\alpha i} |\nu_\alpha\rangle \end{aligned} \qquad \alpha = \mathrm{e}, \mu, \tau \quad i = 1, 2, 3 \tag{1.9}$$

where $|\nu_\alpha\rangle$ is the weak interaction eigenstate
$|\nu_i\rangle$ the mass eigenstate
U the unitary mixing matrix

The evolution of a single state in time is given by multiplication with the time development operator, which in turn contains the Hamiltoinian $\hat{H}$. There the mass eigenstates are very convenient, as the Hamiltonian simplifies to the kinetic energy of the particle

$$|\nu_i(t)\rangle = e^{i\hat{H}t/\hbar} |\nu_i\rangle = e^{-iE_i t/\hbar} |\nu_i\rangle \qquad E_i = \sqrt{p^2c^2 + m_i^2 c^4} \tag{1.10}$$

When plugging this result into the definition of the weak interaction eigenstates given above one gains their time evolution. The transition probability from one flavor eigenstate into another is then given by

$$P(\alpha \to \beta, t) = |\langle \nu_\beta | \nu_\alpha(t) \rangle|^2 \tag{1.11}$$

$$= \sum_i \left| U_{\alpha i} U^*_{\beta i} \right|^2 + 2\mathrm{Re} \sum_{k>i} U_{\alpha i} U^*_{\alpha k} U^*_{\beta i} U_{\beta k} e^{-i(E_i - E_k)t/\hbar} \tag{1.12}$$

The 3-dimensional terms above gets decomposed into three different 2-dimensional terms of two major participating neutrino flavors ν_α and ν_β with their common mixing angle $\theta_{(\alpha\beta)}$

$$\begin{pmatrix} \nu_\alpha \\ \nu_\beta \end{pmatrix} = \begin{pmatrix} \cos\theta & \sin\theta \\ -\sin\theta & \cos\theta \end{pmatrix} \begin{pmatrix} \nu_1 \\ \nu_2 \end{pmatrix} \tag{1.13}$$

The probability to find a neutrino that once was created with the flavor α and the energy E at a distance L with the new flavor β is then given by

$$P(\alpha \to \beta, L) = \sin^2(2\theta) \sin^2\left(\frac{\Delta m^2 L}{4E}\right) \tag{1.14}$$

Experiments investigating those oscillations are in fact only sensitive to this difference in the squared masses

$$\Delta m^2 = \left| m_i^2 - m_j^2 \right| \tag{1.15}$$

One sees that the probability P, of the oscillation isnon vanishing only if the value of Δm^2 is not zero.

As stated above neutrino oscillations have in fact been observed and hencefore a mass difference must exist. So at least one neutrino flavor must neccesarily possess mass. This ultimately has shattered the axiomatic assumption of the zero mass neutrino by the Standard Model!

The experiments mentioned above were able to determine the squared mass difference Δm^2 and the mixing amplitude Θ for the oscillation $\nu_e \rightarrow \nu_\mu, \nu_\tau$ from solar and reactor sources as [Nak07]

$$\Delta m^2_{\text{solar/reactor}} = 8.0^{+0.6}_{-0.4} \cdot 10^{-5} \frac{\text{eV}^2}{c^4} \quad \Theta = 33.9^{+2.4}_{-2.2}$$

Once these quantities are known for all flavors, and the absolute value of one flavour or mass eigenstate is exactly determined, all other values can be computed by the above mathematical framework.
There are 2 scenarios for the neutrino mass eigenstates that might occur:

1. Hierachical order: all masses are below 0.2 eV and greatly differ from each other: $m_1 << m_2 << m_3$
2. Quasi-degenerate order: all masses are above 0.2 eV and similar to each other: $m_1 \approx m_2 \approx m_3$

The determination of the absolute neutrino mass is not only of interest for particle physics. Cosmologists are also very interested in it to settle disputes and validate different theories. They often encounter the neutrino because it has a huge impact on the processes in the early universe and the later state it developed into.
The starting point of this argumentation is the Big Bang: A singularity of immense energy that suddenly exploded into a fast expanding gas ball, which should become our universe. From the huge amount of thermal energy, particle-antiparticle pairs popped into existence and annhilated again in close equilibrium. The energy and mass density during the first development stages were so great that they even macerated the laws of physics: symmetry breakings occured which for example favoured matter over antimatter, leading to the matter dominated universe as we know it.
As the universe expanded further the energy density decreased accordingly. The back and forth creation of heavy particles fell out of equilibrium. This process is also often called 'freeze out' and happened for each type of particle at another time according to their mass and interaction strength. After freeze-out annihilation processes no longer took place and the abundancy became fixed.
As more and more particles fell out of equilibrium and only very light particles remained in the equilibrium state. But eventually also those particles froze out of thermal equilibrium and left the thermal universe only to photons. Aided by cold dark matter gravitational attraction then pulled together stellar matter forming galaxies, stars and planets, forming the visible universe we see today.

Some witnesses of the Big Bang, like the cosmic microwave background (CMB) radiation can still be observed. It originates in scattering processes of photons before the

universe became transparent. The radiation was cooled by the continiuous expansion of the universe and can nowadays be seen at 2.7 K. It is closely related to the neutrino background created shortly before by weak processes in the early universe. These relic neutrinos now are 1.9 K cold, but have a huge density of 339 per cm^3. Their direct detection is still not possible because of their very low cross-section and energy. Nevertheless, the CMB (together with the Big Bang Nucleosynthesis) carries information of some of its traits, what for example enables one to estimate the number of neutrino generations and puts some constraints on the total neutrino mass.
In fact this neutrino background has even greater influence than first thought. Despite their low cross-section, their number and density in the early universe makes them non-negligible in the galaxy formation processes. Their gravitational pull is unable to explain the distorted rotational curves, which which results from cold dark matter.

Where exactly the neutrinos fit in can only be resolved if their mass is better known than it is now. So the determination of the neutrino mass and its important role in different aspects of physics is a burning question. Many experiments try to find a satisfying answer by a variety of approaches. Some of them are dependent on a certain axiomatic model to relate their finding to the neutrino mass. Others are independent of such model but have to cope with heavier systematic influences that are limiting their sensitivity. However, these do not compete but complement each other in a constructive way.
Stated here are first some approaches that are model dependent:

- **Cosmological observations** have yielded a very complex model of the universe, that can relate the current matter distributions back to the fundamental processes at the big bang. The model can then yield characteristics of the neutrino from the dependency on different quantities that are measured in the present universe. For example the BBN can be used to calculate the number of neutrino generations, and together with the CMB it yields an upper limit to the absolute neutrino rest mass.
  This model is often taken as base algorithm for computer simulations that take, among others, the neutrino mass as an input parameter. They extrapolate the development of the universe from its early beginning until its present age (14 billion years) and compare the results to actual observations. These large scale structure (LSS) investigations are a subject of much inquiry because the neutrino mass has a huge impact on the formation process of galaxies.
  The results from cosmology are very sensitive, in particular because of the great abundance of neutrinos in our universe. They are heavily model-dependent and could shatter if the cosmological model should be flawed. Presently favoured is a total neutrino rest mass [Han04] smaller than

$$\sum_i \nu_i < (0.65 - 2)\,\frac{\mathrm{eV}}{c^2}$$

- $\mathbf{0\nu\beta\beta}$, or neutrinoless double beta decay experiments put instrinsic neutrino properties to test. The ansatz is as follows:

In a second order weak process, a β-active nucleus simultaneously converts two neutrons. According to the beta decay reaction, 2 anti-neutrinos should be emitted. In processes beyond the Standard Model, the exchange of a neutrino as virtual particle takes place and nono neutrino would be witnessed. However this can only happen if the neutrino posesses Majorana character, so to say it is its own anti-particle. This would also imply that an emitted right-handed neutrino at one conversion must participate as a left-handed one at the other. The weak force however seems sterile to left-handed neutrinos. This restriction must be loosened accordingly or the neutrino must necessarily have mass to make a broken helicity possible.
If in fact the $0\nu\beta\beta$ decay is observed, the neutrino mass can be calculated from the nucleus matrix element and the isotope life-time. The Heidelberg-Moscow experiment became of special interest here because part of the group reported the successful observation of $0\nu\beta\beta$-events in Germanium, and an according effective neutrino mass of [Kla01] [Kla06]

$$\langle m_\nu \rangle = 0.32^{+0.03}_{-0.03} \frac{\mathrm{eV}}{c^2}$$

This result could neither be confirmed nor refuted yet.

There are also model-independent approaches:

- **Time-of-flight** (TOF) experiments are using the propagation speed of free neutrinos to determine their mass. They simply measure the time it takes for a neutrino of known energy to travel stellar distances. The link is given by the equation for relativistic energy and kinetics

$$E = \sqrt{p^2c^2 + m^2c^4} \tag{1.16}$$

$$p = \gamma m v \tag{1.17}$$

  One still needs a distant cosmic neutrino source that emits neutrinos in a sharp space-time-incident. Supernovae can be used for this purpose because they emit an ultra strong neutrino burst when a star's core collapses and neutronizes. For example in February '87 neutrinos from SN1987A were seen in serveral detectors all over the world and forged the mass limit [Lor01]

$$m_{\nu_e} < 5.7 \frac{\mathrm{eV}}{c^2}$$

- **Investigation of weak decay kinematics** also provides a very feasible approach to the whole problem. These are laboratory experiments and, unlike cosmic approaches, need not deal with model uncertainties. The idea is to study weak decay interactions in which the neutrino participates. Even if the neutrino can not be measured directly at the experiment, its influence is revealed in an unbalanced momentum and energy preservation. The challenge of these experiments is the very tiny signal difference they have to search for in a very broad spectrum.

– The decay can be artificially created in accelerator experiments. There a heavy charged particle decays into lighter traceable particles. A very good example is the pion decay

$$\pi^- \rightarrow \mu^- + \overline{\nu_\mu} \tag{1.18}$$
$$\pi^+ \rightarrow \mu^+ + \nu_\mu \tag{1.19}$$

investigation of which led to the "historic" muon neutrino mass limit of [PDG08a]

$$m_{\nu_\mu} < 0.19 \frac{\mathrm{eV}}{c^2}$$

– Also, it can be a natural decay, like β^-, in which the total energy is measured in a bolometric way. These experiments but need a very sophisticated thermal readout mechanism and extreme cooling. The signal is also influenced by processes on the atomic level. The limit provided by these experiments is at the moment [Arn01]

$$m_{\nu_\mathrm{e}} < 21.7 \frac{\mathrm{eV}}{c^2}$$

– Other experiments which also use natural sources investigate the total decay energy by spectroscopy of the yielded particles. To this category belong the Mainz [Kra04] and Troisk [Lob99] neutrino mass experiments which used the β^--decay of radioactive tritium

$$^3\mathrm{H} \rightarrow {}^3\mathrm{He} + \mathrm{e}^- + \overline{\nu_\mathrm{e}} \tag{1.20}$$

The decay electrons were analyzed in electrostatical spectrometers for their energy near the endpoint. The analysis of these experiments [Ott08] favours an upper limit of

$$m_{\nu_\mathrm{e}} < 2.3 \frac{\mathrm{eV}}{c^2}$$

corresponding to a non obersavtion of a signal with the experiments' maximum sensitivity.

Almost all experiments and approaches predict the neutrino rest mass in the sub-eV scale. The investigation of this regime is the subject of next-generation experiments. The β-decay investigation still remains a very good approach as one can utilize natural sources and is not depending on expensive accelerators. Nevertheless the resolution as well as the signal strength must be further increased, which is difficult as unwanted background effects become a major challenge.

One of the next generation experiments is the project KATRIN.
It carries on in the longline of β-decay experiments and succeeds the Mainz and Troisk experiments. The sensitivity to the neutrino mass will be increased to 0.2 eV. It will use a much stronger β-decay source running on gasous tritium. Furthermore it will use a tandem setup of spectrometers working on the MAC-E filter principle whereof the main spectrometer is 10 m broad to guarantee the best possible energy resolution.

The total setup will be 70 m long and its components will use latest technologies or are themself subjects of research.
The operation of KATRIN is very closely related to vacuum properties. The spectrometers must necessarily operate in high vacuum conditions, while at the other end of the setup tritium gas is continuously injected into the source. Thus, in between a retention system is needed that takes care of the removal of tritium gases and ions. This is the task of the transport section. The module DPS2-F is part of it and entrusted to reduce the effective gas flow by a factor of 10^5 and to simultaneously eliminate unwanted ions. Before KATRIN goes into operation in 2012, all components must be checked thoroughly to varify that the requirements on them are truly fulfilled. This is done in the circumference of acceptance and test experiments. This diploma thesis revolved around these tests and their execution at the module DPS2-F. This thesis was espacially involved in calibration tasks carried out at the reduction-factor setup. The setup is needed in order to validate the capability of the DPS2-F in the removal of neutral gases by pumping. Another center point of this thesis was the development of a next generation ion source. It is needed to test the ion-removal mechanism of the DPS2-F module by generating an ion plasma similar to the one present under live running conditions.

This thesis first presents the framework of the KATRIN experiment and the DPS2-F module before the actual work and contributions to these two fields of research is treated. It is built up as follows

- **Chapter 2** introduces the neutrino mass KATRIN experiment, stating its aim and measurement procedure, and presents the design and functions of the major assembly modules.
- **Chapter 3** pays a closer look to the module of DPS2-F around which the research subjects of this thesis evolve. The design and function is explained in more detail. This directly leads to the test experiments that are performed to verify the functionality by various measurements upon the delivery of the module.
- **Chapter 4** then treats the contributions to the reduction factor measurement which is one of the test experiments performed and tests the module for its capability of tritium gas removal by pumping.
- **Chapter 5** presents the developments and progress on the field of ion sources. These sources are needed for the artificial production of ions to test the capability of DPS2-F in their removal.
- **Chapter 6** summarizes the work done and gives an outlook for the future.

2. The neutrino mass experiment KATRIN

This chapter explains how the neutrino mass will be measured with high sensitivity in the KATRIN experiment. An overview is given on the experimental setup, followed by descriptions of the functionalities and design of the major assembly sections and modules.

2.1 The aim of KATRIN

The **Ka**rlsruhe **Tri**tium **N**eutrino Experiment (KATRIN) (see figure 2.1) is set out to measure the (anti-electron-)neutrino rest mass to a precision of 0.2 eV in a model-independent approach.
KATRIN will analyze the energy spectrum of tritium beta-decay electrons near the endpoint energy where a possible neutrino mass manifests itself. KATRIN will run for 3 years in order to accumulate enough statistics. The measurement with such sensitivity requires highly stable running condition, and a high precision monitoring of the running and control parameters.

The idea of KATRIN was first stated in 2001 [KLI01] as an improved successor of the Mainz and Troisk experiments [Wei99] [Lob99]. The complete setup, once assembled, with a total length of 70 m and a diameter of 10 m at the main spectrometer will be situated at the TLK[1] at the FZK[2] . Currently (July 2009) most components are under construction or testing. Data taking is scheduled to begin in 2012.

2.2 Principle of beta-decay experiments

This section describes how the neutrino mass can be measured by analyzing the endpoint of tritium beta decay.

In a β-decay, a radioactive isotopes looses excess energy in order to gain a favorable atomic-nucleus configuration. There are four kinds of β-decay: β^-, β^+, electron capture and inverse β-decay. All types are moderated by the weak force. This guarantees accessibility to the neutrinos which interact exclusively by the weak force.
The β^- decay (see fig 2.2), which is regulary used in neutrino-mass experiments, is the conversion of a neutron (n) to a positively charged proton (p). To conserve charge

[1] **T**ritium **L**abor **K**arlsruhe
[2] **F**orschung**z**entrum **K**arlsruhe, Leopoldshafen, Germany

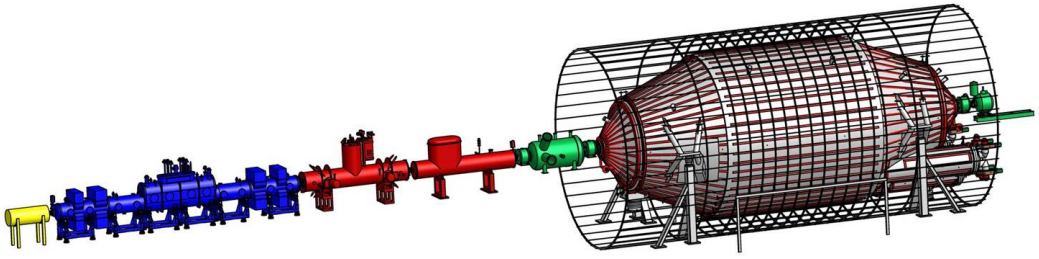

Figure 2.1: **The general KATRIN setup.** The different sections and modules are color coded: Rear wall (yellow), WGTS (blue), transport section (DPS + CPS) (red), pre-spectrometer (light green), main spectrometer (gray), detector (green).

and leptonic flavor, an additional electron (e^-) and electron-antineutrino ($\overline{\nu_e}$) pair is created:

$$n \rightarrow p + e^- + \overline{\nu_e} + E_0 \tag{2.1}$$

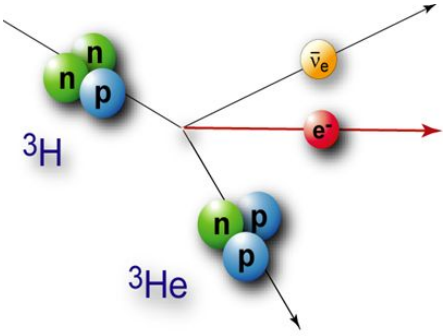

Figure 2.2: **Beta-decay of radioactive tritium.** The atomic nucleus of tritium (^{3}H), which is a hydrogen isotope, consists of 1 proton and 2 neutrons. In the decay process one of the neutrons is converted into a proton forming a ^{3}He nucleus.

The excess energy E_0 from the nuclar transformation is shared among all three participants. The lightness of the electron and the anti-neutrino simplifies the kinematics and enables one to compute the energy spectrum of the β-electrons. The energy spectrum is given by Fermi's theory:

$$\frac{\mathrm{d}N}{\mathrm{d}E} = Cp\,(E + m_e)\,(E_0 - E)\,\sqrt{(E_0 - E)^2 - m_{\nu_e}^2}\,F\,(Z, E)\,\Theta\,(E_0 - E - m_{\nu_e}) \tag{2.2}$$

with the form factor

$$C = G_F^2 \frac{m_e^3}{2\pi^3} \cos^2 \Theta_c\,|M|^2 \tag{2.3}$$

where Θ is the step function

m_e	is the electron rest mass
p	the electron's impulse
F	the Fermi function

When plotted (see figure 2.3) one clearly sees the influence of the neutrino mass at the high end of the spectrum: the function drops rapidly to zero before the endpoint[3] energy E_0 is reached, because the energy difference has gone into the creation of the neutrino.

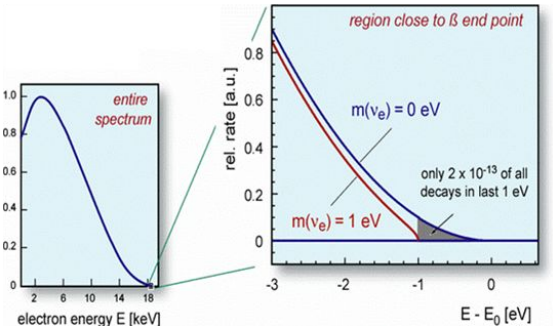

Figure 2.3: **Electron energy spectrum from tritium decay and magnification of the endpoint.** The function rises steeply to a maximum at $\approx 3\,\mathrm{keV}$ and then decreases again to zero intercepting at the endpoint energy. The influence of the neutrino mass is seen at these very high energies by a sudden drop to zero before the endpoint energy $\approx 18.7\,\mathrm{keV}$ is reached. The magnification shows the actual situation for neutrino masses of 0 and 1 eV.

Thereby it is possible to access the neutrino mass by experiments which are able to analyze the undisturbed energy spectrum of the β-decay electrons with high precision. As the counting rates at the very endpoint are very low one parametrically fits the obtained data and deduces the parameter m_{ν_e}. This shows at the same time the greatest challenge of this approach: an improvement to the neutrino mass m_{ν_e} by one order of magnitude requires an increase in sensitivity of the experiment to the observable $m^2_{\nu_e}$ by two orders of magnitudes.
It should again be noted that these experiments use no other input parameters or theoretical models.

2.3 The concept of KATRIN

KATRIN is the next generation β-decay experiment using gaseous tritium as source. It will run a high-luminosity source in combination with very precise spectrometers and detectors supported by a complex component structure to guarantee the success of the

[3] The Θ-function chancels all contributions above the value of its argument, the function ends at the endpoint.

experiment.

The whole experimental setup is pervaded by a magnetic field with strengths between 5.6 T and 0.3 mT, forming out a closed magnetic flux tube. β-decay electrons, as charged particles, are thus confined to cyclotron motion along these magnetic field lines and can thereby be guided from the source, the place of their creation, towards the spectrometers and detector where their energy is analyzed.
The electrons are emitted inside the WGTS[4] where cold tritium gas is injected into the beam tube. The tritium decays in the beam tube, and the β-electrons are guided by the magnetic field in forward direction. At both ends of the beam tube tritium gas is pumped out and recycled. In the forward direction the tritium flow must be further reduced to 10^{-14} mbar l/s. The stage following the source is the DPS2-F[5], which will remove tritium gas by differential pumping and ions by neutralization with dipole electrodes. The beam then passes through the CPS[6] where cold argon frost binds any remaining gas. These measures leave a pure electron beam ready for analysis in high-vacuum spectrometers.
KATRIN will have in fact two spectrometers: a pre- and a main spectrometer. Both are MAC-E filters[7] which allow only electrons more energetic than a given retarding potential to pass by; the low energetic ones are all rejected.
The detector at the end of the setup consists of a segmented silicon detector for counting electrons that were able to pass the spectrometers. The data from the silicon detector then are processed for later analysis along with other information from various sensor and measuring devices.
A parametric fit of the processed data from 3 years of runtime to the form of the β-electron energy spectrum finally returns the neutrino mass.

2.4 Source

2.4.1 Gasous Tritium

The beta decay of tritium

$$^3\mathrm{H} \rightarrow {}^3\mathrm{He} + \mathrm{e}^- + \overline{\nu_\mathrm{e}} \tag{2.4}$$

provides beta electrons with endpoint energy of 18.7 keV for the experiment. Tritium has many advatages as the source for β-endpoint measurements. It is an isotope of hydrogen and shares the same simple atomic structure. The natural bound state is diatomic (T_2), a configuration that allows highly reliable calculations. For example the electronic excitation of hydrogen and tritium states are nearly the same and their boiling point only rises from 20 K to 25 K which becomes important later on. All other properties such as vibrational states and so on can be recalculated with ease.
Tritium has a half-life of $t_{1/2} = 12.3$ y. This allows the construction of a high activity source with a few grams of tritium in a getter storage. The radioactive nature of tritium

[4] **W**indowless **g**aseous **t**ritium **s**ource
[5] **D**ifferential **p**umping **s**ection **2** - **F**orward
[6] **C**ryogenic **p**umping **s**ection
[7] **M**agnetic **a**diabatic **c**ollimation - **e**lectricstatic filter

makes asecondary containment concept necessary. The TLK has the necessary means and expertise to handle this task, motivating the FZK as experimental site.
The use of gaseous tritium instead of a condensed source is also preferrable because source charging can distort the energy spectrum in the latter case. Also the yield rate of undisturbed beta-electrons is limited by the active front area of a condensed source, as most electrons are already stopped inside source before they had the chance to escape, which additionally leads to self charging of the surface and disturbance of the beta energy spectrum by Coulomb repulsion [Bor03].

2.4.2 The windowless gaseous tritium source WGTS

The WGTS is the part where the beta electrons for KATRIN are actually created. The heart is a 10 m long beam tube with a diameter of 90 mm. In the middle an injection chamber is used to inject radioactive tritium gas by small capillaries into the beam tube. The gas itself must be of high purity (95% T_2) and low temperature of only 27 K. It must be injected with a constant inlet pressure of $3.3 \cdot 10^{-3}$ mbar. By a diffusion process the tritium molecules wander to both ends of the beam tube whereby a stationary distribution of tritium in the beam tube is created. This is later on referred to as column-density: the number of tritium molecules per cross-section area unit of the beam line. These are very critical quantities of KATRIN because minor deviations of the column density above 0.2% or the temperature above 0.1% modify the beta spectrum by Doppler effects amd shifts of the energy loss function.
At both ends of the beam tube pumping modules are installed, each consisting of four TMPs[8]. These pump out gases and prevent them from traversing to other systems. The pumped gas is fed to a purification facility of the TLK, where the T_2 content is checked. Unwanted gas remnants such as He, D, and H are removed by gas processing, then enriched by new tritium and finally fed back for reuse in the WGTS. This system is called (inner-)loop. However, these pumping modules are not capable of removing all tritium, which will be removed by other parts in the transport section.
The tritium gas and the beam line must be held at 27 K at the 0.1% level. This precision is maintained by two 2-phase-neon pipes which are directly attached to the beam tube from the outside. These pipes are filled by boiling neon, whose boiling point of 27 K (at 1 bar) allows top maintain the required temperature stabilization.
The beam tube is surrounded by a radiation shield and an isolation vacuum. The superconducting magnets, which use 4 K LHe in cooling and provide the required 3.6 T magnetic field, are mounted outside this isolation vacuum. The magnets are then again surrounded by a liquid nitrogen (LN - 77 K) cold radiation shield and a final isolation vacuum before the outer vessel completes the module.
According to calculations, the WGTS will circulate a constant number of $3 \cdot 10^{19}$ molecules of T_2 inside the beam line, giving a total source activity of $9.5 \cdot 10^{10}$ Bq [Hoe09].

2.4.3 The rear section

Behind the source the rear section is mounted, which is closing off the beam line in backward direction.

[8] **T**urbo **m**olecular **p**ump

The electron beam that is generated by the WGTS is equal in forward as it is in backward direction. Thereby KATRIN can only use half of the activity in the source for the actual measurement process. Electrons from the backward beam as well as those reflected at the spectrometer section hit the rear wall and are neutralized there. The electron beam but still carries valuable information in its spatial and energy distribution. According detector devices in the rear section can thereby explore important properties of the setup during the measurement's runtime.
The rear wall itself is still under development, these are some features that might be included [Mon09]:

- A multiple layer electron detector can determine the total activity of the source. The electrons of the backward beam hit the detector wall and are neutralized, thereby generating a measurable current proportional to the activity. Another complementary measurement is the analysis of bremsstrahlung rays [Mau09].
- A spatially resolving counting detector could be installed, returning the column density in the source. An optional energy resolution might tell about major systematic errors causing disturbances in the energy spectrum.
- An electron gun, a device which can shoot monoenergetic electrons in forward direction, can probe the column density and the transmission function of the spectrometers [For09].

2.5 Energy analysis and electron detection

2.5.1 MAC-E filter

Both spectrometers at KATRIN implement the principle of a MAC-E filter. This method of energy analysis works for all charged particles, which were created in the presence of a magnetic field and is based on the principles of Lorentz- and Coulomb force and preservation of energy and magnetic momentum.

In general, electrically charged particles traverse a magnetic field in a spiral motion. This motion can be split up in one parallel and one orthogonal component to the magnetic field lines, each with an associated energy. This is caused by the effect of the Lorentz-force

$$\vec{F_{\mathrm{L}}} = q\left(\vec{E} + \vec{v} \times \vec{B}\right) \tag{2.5}$$

The parallel component is referred to as the longitudinal energy $E_{||}$; its trajectory is linear tangential to the magnetic field lines.
The orthogonal component is referred to as the transversal energy $E_{\perp}$; its trajectory are cyclotron circles around the magnetic field lines with a given radius $r = \frac{mv}{Bq}$.
The sum of both, the total kinetic energy of the particle, is preserved at all times (if no difference in the electrostatic potential is present)

$$E_{\mathrm{tot}} = E_{||} + E_{\perp} \tag{2.6}$$

Another conserved quantity is the magnetic moment of the particles which is given by

$$\mu = \frac{E_\perp}{B} \tag{2.7}$$

The MAC-E filter uses these circumstances to convert $E_{||}$ and $E_\perp$ into each other in a defined way. This is done by decreasing the magnetic field towards an analyzing plane. As the B-field value drops, so does the transversal energy $E_\perp$, according to equation 2.7. By equation 2.6 this loss in energy is then transferred into the longitudinal energy $E_{||}$. In other words: the velocity parallel to the magnetic field lines increases and the momentum-vector of the particle is shifted closer to the magnetic field lines.
This process is called magnetic adiabatic collimation because in the end all particles which may have started with different momentum-vector angles now face the same direction and fly alongside through the analyzing plane.

The longitudinal energy of the charged particles is analyzed at the analyzing plane. Only particles with kinetic energies above the potential at the analyzing plane can overcome the potential barrier; all other will be rejected. That this only applies for that portion of the kinetic energy that is parallel to the potential gradient ($E_{||}||\text{grad}\vec{E}$). The energy lost to deceleration is converted into potential energy and is retransferred again once the particle leaves the analyzing plane.
This describes the principle of the electrostatic filter, which can sort particles by their kinetic energy.

The MAC-E filter, as it is sketched in figure 2.4, unifies both principles in one setup and thereby creates a reliable sorting mechanism for charged particles:
A magnetic flux tube containing the particles to be analyzed is delivered to a spectrometer vessel. The vessel itself must be kept at extremely high vacuum (10^{-11} mbar) in order to unduce collisions with residual gas atoms. Shaping dipole magnets will then allow the magnetic-field lines to smoothly fan out before they align again at lower magnetic field in the center of the spectrometer and bundle again at the exit. In the central analyzing plane the particles are adiabatically collimated for energy analysis. There are two possible scenarios for each particle: its total kinetic energy is high enough to overcome the potential and flys through the plane; or its kinetic energy is too low and it is stopped before its flight direction is reversed. In both scenarios all particles leave the spectrometer with the same energy they have entered.
The energy resolution of the MAC-E filter is given by

$$\frac{\Delta E}{E} = \frac{B_\text{A}}{B_\text{max}} \tag{2.8}$$

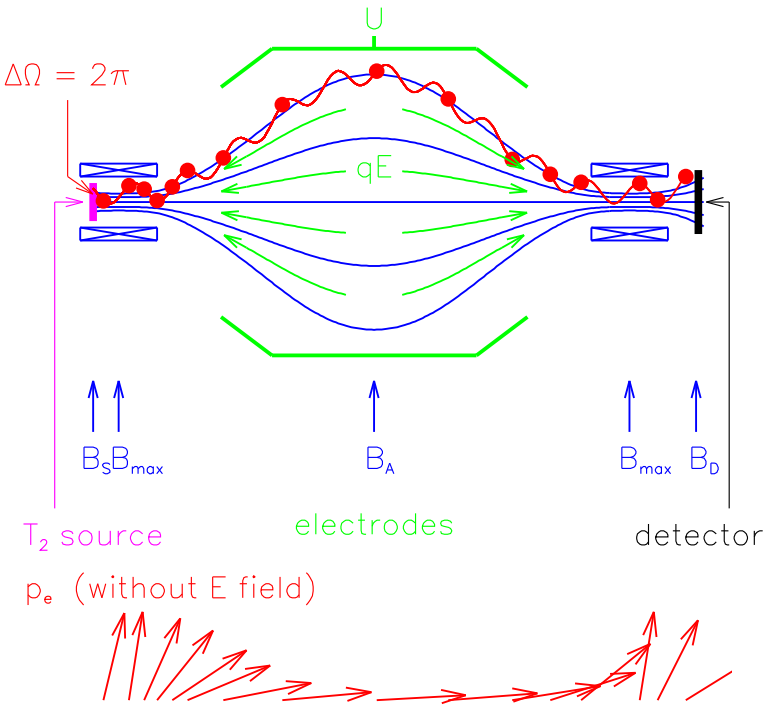

Figure 2.4: **Illustration of a MAC-E filter.** [KDR04] The flux tube with charged particles of various angular distribution is shown on the left-hand side. The magnetic field lines broaden to the analyzing plane in the middle. The particles are collimated; the momentum is directed in forward direction (vectors at the bottom). In the analyzing plane a retarding potential allows only energetic ones to pass. The magnetic field lines then bundle again at the exit reversing the collimation.

2.5.2 Pre-spectrometer

The pre-spectrometer is the system after the transport section and starts off the analysis and detection section of KATRIN. This spectrometer is a vessel of 3.4 m in length and 1.7 m in diameter and operates in ultrahigh vacuum conditions below 10^{-11} mbar. The magnetic field at the central analyzing plane drops to $B_A = 30\,\mathrm{mT}$, which corresponds to an energy resolution of $\Delta E_{\mathrm{Pre}} \approx 100\mathrm{eV}$. Wire electrodes inside the spectrometer create a fixed electrostatic potential of 18.5 keV. The potential is slightly below the endpoint energy. This means that the lower energy part of the beta-electrons is filtered out here, and the flux is reduced by a factor of 10^6. Therefore the pre-spectrometer acts as a rough filter for electrons that are uninteresting for analysis.
The pre-spectrometer has also been a prototype for the much larger main spectrometer. It has been used in the investigation of:

- background by cosmic rays hitting the vessel wall
- background by the formation and ignition of Penning traps
- spectral distortions by electron impact on residual gas atoms
- electromagnetic misalignments
- stability issues of the applied electrostatic potential

To counteract these effects is one of the most demanding challenges of the setup. The pre-spectrometer is ready assembled and has been under testing since 2004.

2.5.3 Main spectrometer

Only the high energy electrons will enter the main spectrometer which is the setup's biggest system with a length of 23.3 m and a diameter of 10 m. (It's delivery in 2005 to FZK was observed as a big public event with great interest in the news [FZK06].)
It works on the same principles as the pre-spectrometer but aims for a much higher energy resolution of $\Delta E_{\mathrm{Main}} = 0.93\,\mathrm{eV}$. In contrast to the pre-spectrometer its retarding potential is not fixed but adjustable in the range between 18.5 keV and 18.8 keV in order to scan through the endpoint energy.
The increased volume requires the introduction of new measures to counteract unwanted effects. An air-coil system with additional shaping coils is used to align the magnetic lines. Also the maintenance of the ultrahigh vacuum conditions in such a huge volume requires very strong TMP and NEG-pumps.

2.5.4 Main detector and other monitor devices

The main detector consists of a highly durable silicon semiconductor with a 4-fold segmented center plate surrounded by 12 rings with 12 pixels each. Each pixel covers the same area. The detector must be able to measure the rare events above 18.5 keV which occur at a rate below $< 10\,\mathrm{mHz}$ with high sensitivity. This requires robust background suppression, including passive shielding and a sophisticated veto system in the detector

itself.
The detection rate for each retarding potential is saved to a computer system for later evaluation and analysis.

Additional data from monitoring devices are required for the analysis of the β endpoint. These monitoring devices include:

- A monitor spectrometer, which is connected to the main spectrometer's high voltage supply. Equipped with a calibrated source and detector, it is used to monitor the voltage stability of the retarding potential.
- A forward beam monitor, which can move through the beam, is situated before the energy analysis section. It is used to determine potential inhomogeneities in the column density or magnetic misalignments of the transport section.
- The overall source activity can be measured by the main detector, when the retarding potentials at pre- and main spectrometer are reduced.
- A system based on laser Raman spectroscopy (LARA) continuously measures the isotopic content of tritium in the circulated gas.
- Temperature, pressure, magnetic, voltage and other sensors monitor the stability of their respective quantities at various positions throughout the setup.

2.6 The transport section

The transport section is situated between the source and the energy analysis section. It is used to guide the electrons to the spectrometers and to reduce the gas and ion content in the electrons' path.

2.6.1 The differential pumping section DPS2-F

The DPS2-F is the first module of the transport section. The β-electrons are delivered to its entrance, which is held at a magnetic field of 5.6 T by superconducting magnets. The electrons are guided through an angled tubing system where four strong TMPs (Leybold MAG2800) are mounted. They pump out gas, and reduce tritium content and residual gas pressure along the beam line. The DPS2-F was designed to achieve a reduction of the tritium flux by 10^5 [Bon03].
The other objective of the DPS2-F is the removal of ions that are also simultaneously created in the WGTS. They are likewise guided by the magnetic flux tube and their removal is much harder. This is done by dipole segments inducing an $E \times B$-drift that pushes the ions to the dipole walls where they are neutralized [Rei09].
The DPS2-F is also equipped with two so called FT-ICR[9] traps [Dia09]. These allow the measurements of the ion current entering and leaving the DPS2-F module.

[9] **F**ourier **t**ransformation - **i**on **c**yclotron **r**esonance

2.6.2 The cryogenic pumping section CPS

The last part of the transport section is the CPS module, which acts as a huge getter pump to remove the residual tritium gas.
Electrons enter this system through the guiding of a 5.6 T magnetic field from a superconducting magnet. The surface of the tube is at liquid Helium temperature (4 K) and is covered by a very thin layer of argon frost. The cold argon layer is used to cryosorb the colliding tritium molecules onto its surface. Thereby the gas flow is reduced by another factor of 10^7 so that the tritium partial pressure drops below 10^{-20} mbar.
Because the CPS accumulates an increasing amount of tritium during runtime, a regular regeneration cycle must be held.

3. Planned test experiments with DPS2-F - an overview

After introducing the concept and setup of KATRIN the focus will now be on the DPS2-F module. The thesis at hand and the projects involved evolved mostly around this special component.
During the writing of this thesis, the DPS2-F was still under assembly and was completed and delivered to the FZK in July 2009. But before this cryostat or any other part of KATRIN can be accepted in the closed setup, it must be individually checked and tested if it truly fulfills the expected specifications. This is of importance because otherwise one would endanger the measurement with the aspired sensitivity.

This chapter will take a closer look at the tests of the DPS2-F, which are the magnetic guidance of β-electrons and the removal of tritium gas and ions. To set this into context, a more detailed description of the DPS2-F setup is given ahead. The following sections deal with the actual test measurements that must be performed: acceptance tests, measurement of magnetic alignment, gas flow and ion reduction capability and also the testing of additional monitoring devices such as the FT-ICR trap.

3.1 DPS2-F - a close-up look

The DPS2-F was designed for two key tasks of the experiment: The removal of unwanted particles, and the undisturbed guiding of beta electrons. These rather simply formulated objectives get rather complicated when broken down to the very components and physical principles at work.

3.1.1 General design

The heart of the DPS2-F is the beam line with a diameter of 86 mm which is broken up into five pieces of 1 m lentgh each (see figure 3.1). Each two succeeding pieces are tilted by 20° to each other and welded to a vacuum cavity, the pumping port. By the angled design a direct line of sight from the WGTS to the spectrometers and detector is prohibited to prevent molecular beaming. Liquid nitrogen keeps the beam line and pump ports at a constant temperature of 77 K. All five tube segments are surrounded by superonducting magnets (see figure 3.2), which must be kept below their transition temperature. This is achieved by liquid helium cooling and thermal isolation from the exterior by vacuum. The magnets rest on a support structure welded to the outer liquid nitrogen cold radiation shield; magnets do not touch the inner beam line at any point. The support structure itself is very robust: the tilt of the tubing and magnets induces

strong torque moments under operation because the magnets try to align themselves. An isolation vacuum then isolates the entire inner structure from the outer hull.
A lot of additional tubing is necessary to provide the cooling gases, their feed and carry-off. This is done through a turret on top of the cylindrical DPS housing. Situated there are connections for this purpose, but also safety gas releases and electrical connectors to sensors, which are attached to the inner setup at various places. These monitor pressure, magnetic field and temperature.
The connection of the beam line to neighboring modules is done by 250 CF flanges and gate valves that can close off the setup if necessary. In addition to the pumps, the DPS2-F also houses FT-ICR traps and dipole elements inserted in the beam line.

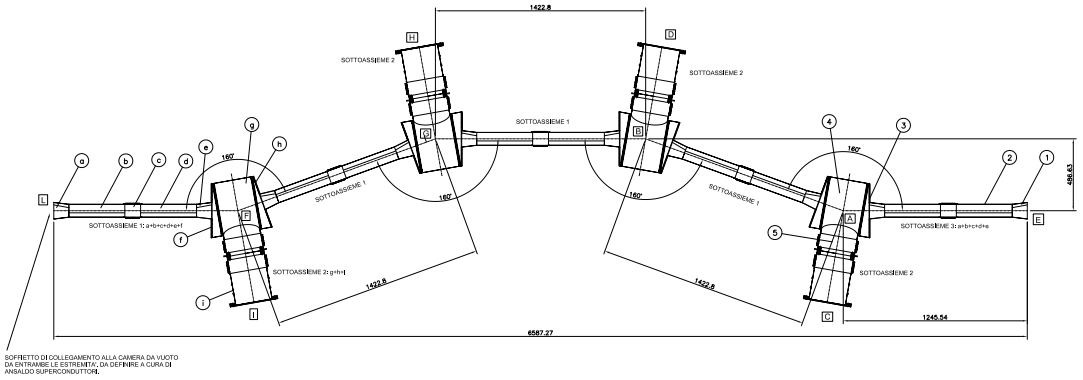

Figure 3.1: **Drawing of the inner beam line of the DPS2-F by the manufacturer.** The illustration shows the beam line being designed and manufactured by ASG. Clearly seen are the five tubing segments tilted by 20 degree against each other and the pump ports at the intersection points.

3.1.2 Pumps

Each of the four pump ports is equipped with a Leybold MAG2800 TMP with a nominal pumping speed of $S = 2000\,\mathrm{l/s}$. The gas flux of $q_{\mathrm{in}} = 10^{-2}\,\mathrm{mbar\ l/s}$ which enters at a pressure of roughly $p_{\mathrm{in}} = 10^{-5}\,\mathrm{mbar}$ is reduced by each sequential pumping port by approximately a factor of 20, until after the last one only a flux of $q_{\mathrm{out}} = 10^{-7}\,\mathrm{mbar\ l/s}$ at a pressure of $p_{\mathrm{out}} = 10^{-9}\,\mathrm{mbar}$ remains [Bon03].
These are but design values and depend on the performance of up- and downstream modules like DPS1-F and CPS.

3.1.3 FT-ICR traps

The DPS2-F will house two FT-ICR[1] ion traps; one at the entrance and one at the exit. An FT-ICR trap (see figure 3.3)uses both a magnetic field and an electrostatic potential to trap ions in an enclosed space. By radio frequency excitation of the ions' cyclotron

[1] **F**ourier **T**ransformation - **I**on **C**yclotron **R**esonance

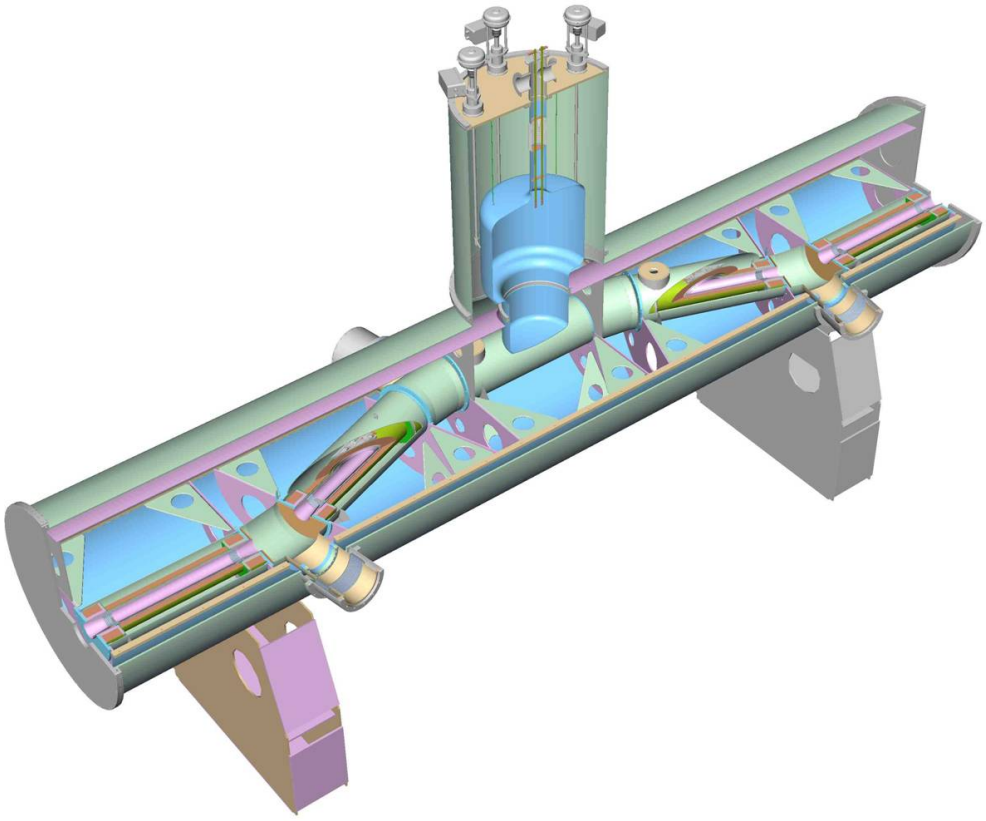

Figure 3.2: **Illustration of the DPS2-F module with inner components and beamline.** Shown is the DPS2-F module with a quarter cut along the center to reveal the inner components and support structure. The turret on top enables the supply of cooling gases and the pumping of the isolation vacuum cavities.

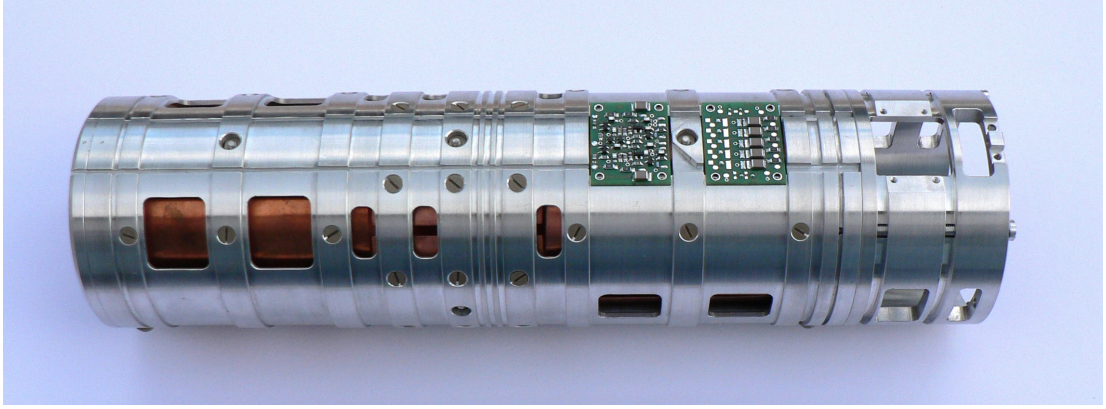

Figure 3.3: FT-ICR Trap fully assembled

eigenmotion, the trap is able to return a spectral analysis of the ion composition by the charge-mass-ratio.
The measurement itself is not invasive, so that the monitoring of the ion flux can be performed during the runtime of the experiment.
The FT-ICR traps for KATRIN are provided by Stahl Electronics GmbH and are tested and developed at MPI-K Heidelberg [Dia09].

3.1.4 Dipole elements

Specific dipole elements are inserted in the middle three tube segments that take care of the ion removal. This is done by an applied orthogonal electric gradient. It pushes charged ions via an $E \times B$-drift to the outer walls where they are neutralized. The former ions can then, as neutral particles, be pumped out along with the other gas [Rei09].

3.2 Acceptance tests upon delivery

The DPS design and specifications were ready in 2004 and the manufacturing contract signed with ASG[2]. In the beginning of 2009 the module was assembled and ready for testing to check if the required specifications are fulfilled by the completed module. These acceptance tests check the correct assembly and validate the proper operation.

3.2.1 Vacuum tightness

The complete KATRIN setup operates under vacuum conditions. Therefore it is of major importance that every part of the beam line meets the specifications on the vacuum tightness. The DPS2-F furthermore operates in the tritium-related section. A possible vacuum breach might cause the leak of radioactive gas out of the beam tube into the cryostat vessel. That is why every weld and vacuum connection must be thoroughly tested by leak detectors and the overall tightness of the beam tube system has to be

[2] **A**nsaldo **S**uperconductori **G**enua, Italy

probed.

Preliminary tests were already done at the ASG manufacturing site, but a repeated test after the shipping and cooling-down is in order. An endpressure of 10^{-9} mbar must necessarily be achieved.

3.2.2 Temperature

Another key parameter are the temperature margins throughout the module. Every margin must be met in order to guarantee functionality of DPS2-F. Especially the beam line temperature of 77 K must be stable. Also, the continuous LHe cooling of the superconducting magnets must be assured under all circumstances. Insufficient cooling and local breach of the superconducting transition temperature results in the quenching of a single magnet module, which is most undesirable.
Even the cooling-down and warming-up process must be operated carefully. If performed too fast, both introduce local temperature gradients that put stress on the welding and support structure by thermal expansion or shrinking.

As a first step, a suitable cooling-down schedule was developed in correspondence with the manufacturer, who is familiar with the setup and experienced with the cryogenics involved. The cooling-down is then carried out but closely monitored in every step by sensors and personnel, if necessary the procedure is modified. Multiple temperature sensors are installed throughout the setup, most of them redundant, to report the temperature. Their correct operation and rigging is checked simultaneously.
The complete cooling-down is expected to take at least three weeks whereby the system should be at running conditions. Only then some of the internal components are switched on individually and the heat load introduced by their operation is monitored. This information helps to work out safety guidelines and slow control safety circuits to ensure the proper operation of DPS2-F.

3.2.3 Electrical connectivity and integrity

Another test performed is the electrical connectivity and integrity check. Because the DPS2-F is a very complex system with lots of sensors and small electrical components every one must be connected correctly to the control devices. A misconnection might destroy sensors that are embedded deep inside the system and cannot be exchanged easily. Also the insulation and conductivity of all cables must be given.
The DPS2-F beam line and housing must be insulated in order to make it possible to apply an electric potential during operation; implying that the electrical integrity of DPS must be assured with all connected pump tubing and external components.

The test of all the above is quite extensive because of the amount of connections that must be checked. A first test under warm conditions will be done, where it is still possible to open the setup and do changes. After the test is concluded to satisfaction, a rough second check is performed when the setup is cold.

3.2.4 Magnet stability

The stability of the magnetic field inside DPS2-F during runtime is also very important. All four magnets must provide the specified strength of 5.6 T to allow normal operation. A decrease above 10^{-4} over 3 month must not be exceeded.
The test of the magnet stability will require that additional magnetic sensors (Hall probes) are put in place inside and outside DPS. The DPS2-F is then closed and evacuated. The setup is brought to running conditions and the superconducting magnets are ramped up. The system is then left in stand-alone mode for at least 2 weeks and the decrease of the magnetic field is monitored and evaluated in short intervals.
Intentional magnet quenches must also be performed to test the safety measures of the module if such a situation might occure during the operation of the experiment.

3.3 Measurement of magnetic alignment

One of the main tasks of DPS2-F as part of the transport section is the guiding of the β-electrons by the inner magnetic flux tube. The beam should be delivered like it entered, and no disturbance or alteration should occur during the transport. Clearly this property must be validated under conditions similar to the actual experiment.

For this test, a movable e-gun will be installed at the entrance of DPS2-F which is able to create electrons with specific energy. At the exit a pixel detector or similar will be installed. The DPS2-F is then brought to running conditions and the superconducting magnets raised to 5.6 T.
The electron gun will then shoot electrons with different energy and angular distributions in the magnetic flux tube whereby the whole cross-section of the beam tube is probed [Schw09]. The detector at the other end should then register the same number of electrons on the same unit area they were created upon by the e-gun. If this is not the case the magnets need additional attunement and reevaluation until the results are satisfactory.

3.4 Measurement of gas flow reduction

Another major task of the DPS2-F or the transport section in general is the removal of excessive neutral gas, expressed by the reduction factor. Otherwise it would not be possible to maintain the high vacuum conditions and the low background rate at the spectrometer section. A pressure above the design value would result in an increased amount of tritium to get to the CPS, which must make up any DPS shortcoming and must retain the excessive tritium by capturing. In this case a shortened regeneration period would be the result. The worst case would be the migration of tritium inside the spectrometers. There it would contaminate the vessel permanently by diffusion in the metal grid of the hull, leading to a highly increased background level which would render KATRIN inoperational. Therefore the address of this property is highly important.

The reduction factor is a main subject of this thesis and is treated in full length in chapter 4.

3.5 Investigation of plasma properties

In addition to neutral gases DPS2-F has also to deal with charged particles from the WGTS that must be removed likewise. Their removal is a lot trickier: unlike the neutral gas ions cannot simply be pumped out, because they are confined to cyclotron motion which limits their radius of action. The threat they pose to the setup is even worse then the one of the neutral gases: Tritium ions have a high substitution probability with any material they come in contact with. Their presence in the spectrometers also could enable the filling and possible ignition of Penning traps, which would increase the background level and prohibit a high sensitivity measurement.

3.5.1 Ion creation in WGTS

The main purpose of the WGTS is the creation of great numbers of undisturbed β-electrons from tritium decays. The greater the tritium density in the beam line, the greater is the β-electron luminosity. This comes at a price: in the tritium beta decay also positive charged helium cores ($^3He^+$) are created. These generate stable plasma as they are captured by the magnetic field lines and their recombination probability is limited. The beta decay reaction on molecular level reads

$$\text{beta-decay} \qquad T_2 \rightarrow \left({}^3\text{HeT}\right)^+ + e^- + \overline{\nu_e} \tag{3.1}$$

The electrophile helium atom tends to break up the remaining bond to the associated tritium atom by stripping its electron. In the presence of additional tritium gas in the perimeter charged tritium clusters eventually form which can grow upon the association of additional tritium molecules. Conceivable are also electron impact induced reactions which lead to the formation of new anion and kation species.
The table below states some of the reactions that take place

$$\text{helium dissociation} \qquad \left({}^3\text{HeT}\right)^+ + T_2 \rightarrow {}^3\text{He} + T_3^+ \tag{3.2}$$

$$\text{electron impact ionization} \qquad e^- + T_2 \rightarrow T_2^+ + 2e^- \tag{3.3}$$

$$\text{electron impact dissociation} \qquad e^- + T_2 \rightarrow T + T^+ + 2e^- \tag{3.4}$$

$$\text{(radical) substituation} \qquad T_2^+ + T_2 \rightarrow T_3^+ + T + 1.17\text{eV} \tag{3.5}$$

$$\text{electrophile dissociation} \qquad e^- + T_2 \rightarrow T^- + T \tag{3.6}$$

$$\text{cluster formation} \qquad T^+ + T_2 \rightarrow T_3^+ \tag{3.7}$$

The creation of rather stable ions is supported by the low energetic thermal environment at low pressures and limited action radius, which suppresses recombination and other number limiting processes.
The ion flux from the WGTS is expected to be in the order of $0.6 \cdot 10^{12}$ ions per second or in other words 100 nA [KLI01].

3.5.2 Test of plasma properties

The capability of the DPS2-F to remove these ions must be tested likewise. The device responsible for the removal are the three dipoles that are inserted inside the DPS which neutralize them (see section 3.1.4). The removal mechanism depends on the presence of a magnetic field which is why a suitable test can only be conducted under cold running conditions.
In this circumference the two FT-ICR traps are very useful. They can in realtime measure the amount of ions at the entrance and exit of DPS2-F. The position of the dipoles in between them enables the conclusion of the removal capability.

During the acceptance tests the DPS2-F is still a stand-alone and closed-off setup. This is why one needs a compact source of some kind that can be attached to the entrance flange of DPS2-F and provide an ion plasma similar to WGTS.
Such a commercial source could not be found and the development of an ion source was subject of earlier research and also of this diploma thesis. Chapter 5 is especially dedicated to treat this matter.

4. Contributions to gas flow reduction factor measurements

The preparation for the DPS2-F reduction factor measurement was already on the way as the circumference of this thesis began. The DPS2-F was scheduled to arrive in mid-2008, why the conclusion of the assembly and calibration tasks of the test setup became a pressing issue. This diploma thesis was thus involved in the calibration measurements and beyond.

This chapter will present the principle of the reduction factor measurement and how it is put into action at the DPS. A detailed description of the test setup is given before the calibrations of the involved components is stated. The following sections then probe further properties of the measurement concept and investigate an alternative approach by the utilization of a leak detector. The chapter concludes with a summary and feasibility assessment for the reduction factor measurement at DPS2-F.

4.1 Purpose and work principle

As explained in section 3.4 it is important to know to what extent the DPS2-F is able to remove neutral gases. The corresponding quantity for this retention capability is the so called reduction factor[1]. It is the ratio between the gas flow that enters the DPS2-F (Q_{in}) and the one at the exit (Q_{out}).

$$R = \frac{Q_{\text{in}}}{Q_{\text{out}}} \tag{4.1}$$

This quantity can be determined by comparing measured output flow to the flow injected at the input by a suitable system. Despite the fact that the configuration of DPS2-F is fixed by design, the value of R is not. It heavily depends on the conditions at the so called boundary surfaces: inlet, outlet and the 4 pumping ports and the components installed there. Different pressures, pumping speeds and gas mechanical quantities influence each other and the overall performance of the module. An important quantity in this context is the gas capture capability C of a given surface. It states the probability of a specific gas particle to be captured on one of the boundary surfaces upon impact and its removal from the equilibrium. This quantity is used to model TMPs in simulations by X. Luo[Luo05] of DPS2-F. They return the design tritium reduction factor of $1.3 \cdot 10^5$.

[1] german: **U**nterdrückungs**f**aktor

On the practical level the experimental access of this quantity has some technical issues: The use of radioactive tritium for test measurements is not feasible without a closed loop set-up. Any substitute processing gas has a gas kinetic differimg from tritium and changes the DPS2-F's performance. Also, for an exact measurement the same boundary conditions must apply like during the real experiment: At the inlet flange the same pressure and gas flow must be present as if the WGTS would be connected and the same capture factor must apply. The same applies in respect to the CPS at the outlet flange. Both requirements are quite complicated without using the actual cryostats because the synthesis of their respective performance parameters is known only by way of simulations.

The performance of every source-related cryostat in the KATRIN setup is designed for tritium operation. But because of the radioactive nature its use is impractical. A good substitute is deuterium which is a stable hydrogen isotope with comparable gas kinetics. Deuterium is therefore used in the reduction-factor measurement along other inert processing gases like helium, neon, argon and nitrogen for interpolation to tritium. Helium occupies here a special position, because with the mass of 4 amu it has the same mass as the deuterium molecule.

DPS2-F is supplied at the input with a stable gas flow and pressure by utilization of a flow controller. The expected flow at the output is 10^{-7} mbar l/s. A system equipped with a cryopump at the exit of DPS2-F captures and accumulates transmitted gas. After a time period (t) of 2–3 days the gas collection is stopped and the pump warmed up. The captured gas is then released back into the volume (V_{release}) where it creates a pressure (p) of the order 10^{-3} mbar. This allows the determination of the transmitted gas amount.

Key components of the setup must be carefully calibrated and some characteristics of the vacuum system, e.g. the release properties of the cryopump, must be known in detail. Outgasing from the cryopump represents background to the measurement that requires correction. Therefore the setup houses an RGA[2] which can correct this on the basis of the gas composition and the contained fraction of the processing gas (f). Thereby the correct gas flow at the output can be determined as

$$Q_{\mathrm{out}} = \frac{p \cdot f \cdot V_{\mathrm{release}}}{t} \tag{4.2}$$

[2]Residual gas analyzer

4.2 The test setup

This chapter will introduce some abbreviations to name involved vacuum components as it is custom at the TLK. These are made up of a prefix letters stating the operation of the device and a three digit serial number to identify each component. Table 4.1 states important abbreviations for the reduction-factor setup.

Table 4.1: **Important abbreviation for vacuum components and their German and English names**

Abbr.	german	english
HV	Handventil	Manual valve
RV	Reguliertes ventil	Regulated valve
AV	Automatisches Ventil	Automated valve
VP	Vakuumpumpe	Vacuum pump
RT	Temperatursensor	Thermal sensor
RP	Drucksensor	Pressure sensor

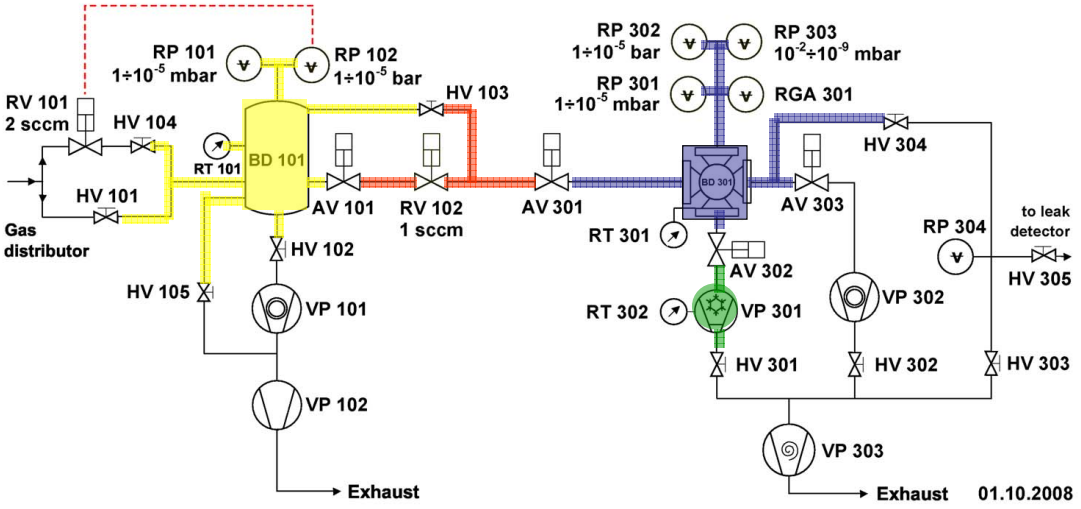

Figure 4.1: **Flow and component chart of the reduction-factor setup.** Different volumes are marked by color regarding their use: the injection buffer (yellow), the DPS feed through with flow controller (red), the expansion volume (blue), the cryopump volume (green)

4.2.1 Injection system

The injection system can be seen in the figure 4.2 and on the left side of the flowchart in figure 4.1.
The heart of the injection system is the 15 l buffer vessel with the connected pressure

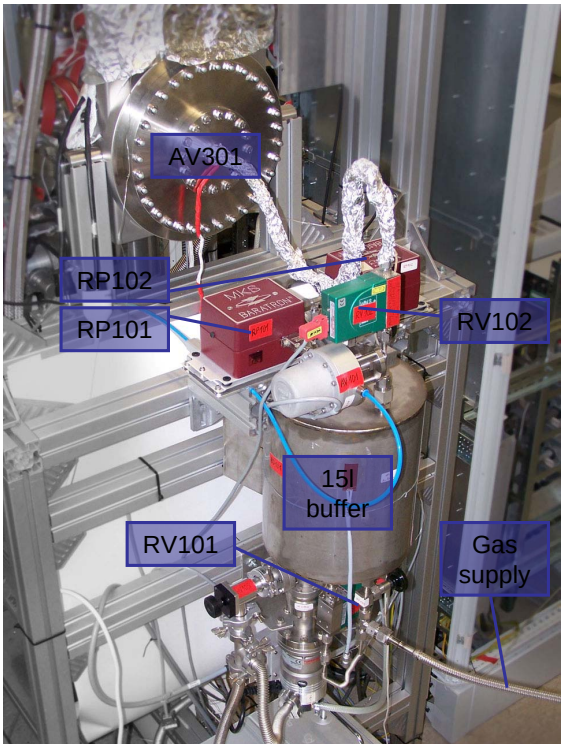

Figure 4.2: **The injection system.**

gauges RP101 (Baratron, MKS 690A01TRA, range 10^3–1 mbar) and RP102 (Baratron, MKS 690A13TRA, range 1–10^{-3} mbar). The vessel is connected to a gas cupboard, which supplies the setup with different gases like deuterium at a nominal pressure of 1 bar. The connection is done via the flow controller RV101 (MKS M200-02C4V2A, range 2 sccm[3]), which is rigged to the pressure gauge RP102 (MKS M200-02C4V1A, range 1 sccm). Thereby it is able to open and close accordingly to the actual pressure in the buffer vessel and thereby maintain a constant pressure. The gas injection is done via the flow controller RV102, which has an internal gas flow determination mechanism (heat conduction) and opens to a preset gas flow value.
For evacuation the TMP VP101 (Leybold TW70, end pressure 10^{-10} mbar) in combination with the prevacuum pump VP102 (Adixen/Alcatel ACP15) is connected to the buffer vessel in order to evacuate the setup and flush out unwanted gases.
Different manual and automated valves conclude the system and close it off.

4.2.2 Collection system

The injection system can be seen in the figure 4.3 and on the left side of the flowchart in figure 4.1.
The collection system is based upon a central six-cross piece. It provides enough connection options for all of the different devices needed for the measurement. It also makes up 70% of the later release volume and allows the nearby installation of sensor

[3]standard cubic centimeter, = 0.018124 mbar l/s

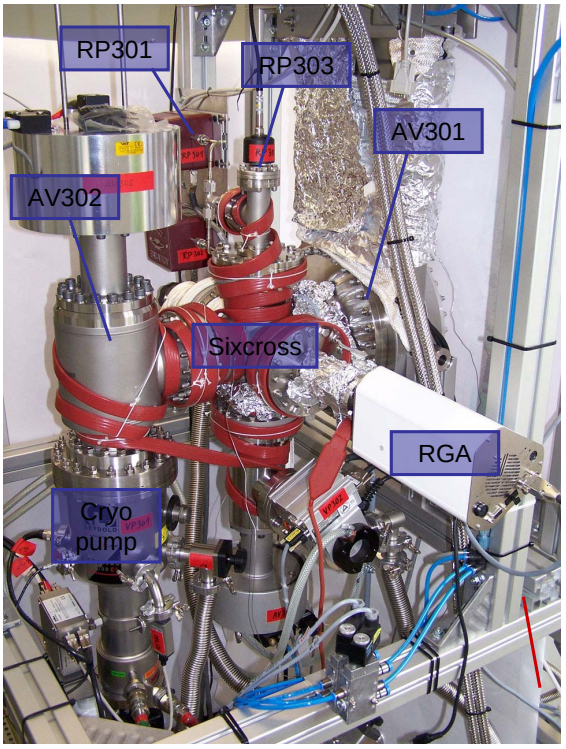

Figure 4.3: **The collection system.**

devices by its big flanges.
On the lower flange the automated valve AV302 and cryopump VP301 (Leybold COOLVAC 800CL, end pressure 10^{-10} mbar) are mounted. The latter is connected to a helium refrigerator in order to achieve the low cold head temperature of 8 K and make it able to capture hydrogen like molecules (deuterium evaporation point 25 K). Another flange is equipped with the three pressure gauges RP301 (Baratron, MKS 690A01TRA, range 10^{3}–10^{0} mbar), RP302 (Baratron, MKS 690A13TRA, range 10^{0}–10^{-3} mbar) and RP303 (Leybold RP27, range 10^{-3}–10^{-10} mbar), which in combination cover from atmospheric pressures down to 10^{-10} mbar. The rest gas analyzer RGA301 (Pfeifer QMS 200 Prisma) is installed at another flange.
The last flange is closed by the connected TMP VP302 (Leybold TW70, end pressure 10^{-10} mbar) and combined prevacuum pump VP303 (LeyboldSC15D), which aid in the evacuation and regeneration process of the cryopump.
Different manual and automated valves conclude the setup and allow the definition of different sub-volumes.

4.2.3 Additional components

The setup is controlled via a computer based slow control which allows the simultaneous recording of read-outs, the fast operation of the automated valves and development of safety interlock routines. The RGA is also operated by a computer program, which also provides data editory tools.

The maintenance of clean vacuum conditions at the experimental setup is very important: Surface adhesious gases (water vapor, hydrogen) are especially hard to remove once they are gettered in the cryopump. So after the experimental assembly, a thorough bake-out was done. Before every measurement the injection system needs to be flushed with the test gas to be used.

4.3 Calibration measurements

As mentioned before, all key devices of the setup must be calibrated before the reduction factor measurement can be performed. To do so the injection and collection system were conjoint in one setup, so that the one system could be calibrated by the other and vise versa.

This section will present the calibration measurements of the volumes, cold cathode Penning gauge, flow controllers, the RGA and also the release properties of the cryopump.

In these measurements the readings of the Baratron devices were considered to state the true pressure inside the system. This is justified because these Baratrons, which are aneroid gauges, measure the change of capacity in a thin membrane that is induced by the pressure forces on the surface. This principle of the measurement is independent of the gas chemistry and based only upon the very definition of pressure. Their use is however limited to pressures above 10^{-3} mbar.

4.3.1 Volume calibration

For the full report on this task please refer to [Got08].

Definition of volumes

To perform quantitative measurements with gases it absolutely necessary to have exact knowledge about the volumes involved at the vacuum setup. The following volumes have been denoted stating their outer boundary components:

1. V_1: injection volume (yellow in figure 4.1)
   Front: HV101, HV104
   Back: HV103, AV101
   Pump: HV105, HV102
2. V_2: feed through (red in figure 4.1)
   Front: HV103, AV101
   Back: AV301
3. V_3: collection volume (blue in figure 4.1)
   Front: AV301
   Back: AV302
   Pump: AV303, HV304

4. V_4: cryopump (green in figure 4.1)
   Front: AV302
   Pump: HV301

All these volumes are well defined and separated by tightly closing valves. The gas expansion technique was used to determine their enclosed volumes.

Gas expansion technique

The gas expansion technique utilizes the difference in pressure and temperature when a specified amount of an inert gas is expanded to compare the volumes involved. If the processing gas obeys the ideal gas law, the new volume can be computed by the formula

$$V' = \frac{T'}{T} \cdot \frac{pV}{p'} \tag{4.3}$$

$$V_{II} = \frac{T'}{T} \cdot \frac{pV_I}{p'} - V_I \tag{4.4}$$

where $V\,(')$ are the old (V_I) and the new volume ($V_I + V_{II}$),
$T\,(')$ are the temperatures and
$p\,(')$ the pressures before and after the expansion

As most vacuum systems can be made up from various volumes, all of them can be calibrated against each other in order to minimize possible systematical errors. However, not every volume is equipped with pressure and temperature sensors, thus limiting the number of possible combinations.

Measurement and Calculations

Before beginning the calibration procedure the whole system was baked out, checked for outgasing from the surfaces and evacuated. The initial pressures were chosen in the region of $100 - -900\,\mathrm{mbar}$. This guarantees a minimal systematic error on the pressure readings, as the levels from outgasing are many orders of magnitude below the measured pressure regime.
In order to serve as reference the gas inlet volume V_1 was calibrated by a different method as described above: A gas can of known volume V_0 filled with a weighted amount of Xenon (Xe) was connected to the gas inlet volume V_1. Using the law for molar gas weight

$$M = \frac{m}{N} \quad M_{\mathrm{Xe}} = 131.293 \frac{\mathrm{g}}{\mathrm{mol}} \tag{4.5}$$

and the ideal gas equation one substitutes in equation 4.4 to gain

$$V_1 = \frac{mkT'}{Mp'} - V_0 \tag{4.6}$$

As only V_1 has a direct gas supply and thereby has a well known volume it is preferred as original volume for all other measurements. These are the volumes found after repeated measurements:

$V_1 = 15.41\text{l}$
$V_2 = 9.56(2)\text{l}$ using $V = V_1$ and $V' = V_1 + V_2$
$V_3 = 10.20(33)\text{l}$ using $V = V_1$ and $V' = V_1 + V_2 + V_3$
$V_4 = 4.66(1)\text{l}$ using $V = V_1$ and $V' = V_1 + V_2 + V_3 + V_4$

4.3.2 Flow gate and pressure gauge calibration

The flow controller RV102 as well as the pressure gauge RP303 also needed calibration. The calibration method used made it possible to calibrate both devices simultaneously by utilizing the accurate readings of the Baratron pressure gauge RP301 and other traits of the setup. It was also possible to simultaneously record data that was valuable in the calibration of the RGA later on. The data aquistition system allowed the recording of the neccessary data.

4.3.2.1 Determination of real gas flow

The pressure (p) in a certain volume (V) is given at all times by the flow (Q) of gases in and out of the system. When the gas flow is linear this is represented by the equation

$$p\,(t) = p\,((t = 0) + \frac{Q \cdot t}{V} \tag{4.7}$$

This relation was utilized to determine the real flow of gas through the flow controller RV102 into the collection volume and to compare it to the read-out value.

Measurement via pressure rise

The setup is first prepared for the measurement: The flow controller is completely closed, the injection volume is brought to a level of about 10^2 mbar of the processing gas. The collection volume however is evacuated and the TMP is kept running.
Then the flow controller is slightly opened to a preset value (Q_{RV201}), allowing gas to flow into the collection volume. The running TMP establishes a pressure gradient generating a stable local pressure (p_0) at the readout devices. A reading of the RGA is taken and the pressure stated by RP303 is noted.
The actual measurement begins when the pumps are closed off. The data acquisition system is started and the timestamp noted as $t = 0$. As gas is no longer pumped out of the volume it slowly fills up, the pressure rises. This process proceeds for an adequate time, so that the pressure can rise into the regime where readings of RP301 can be taken ($> 10^{-3}$ mbar). However the process stops before the pressure in the collection volume becomes comparable with the one in the injection volume.
After the measurement is concluded the setup is brought back into the initial state and a new dataset for a different preset value or gas type is taken.

The calibration curves were worked out by A. Gotsova and can be found in [Got09] and [Luk09a].

4.3.2.2 Determination of pumping speed

The pumping speed (S) is independent of pressure in the molecular flow regime. It states the linear relationship between the local gas flow (Q) and pressure (p)

$$S = \frac{Q}{p} \tag{4.8}$$

The assessment of the pumping speed of the TMP VP301 at the center of the six-cross was not mandatory. It could but be used to access properties of the molecular flow regime that could be exercised to lower pressures and thereby calibrate e.g. the cold cathode pressure gauge.

Measurement via pressure gradient

The setup is then prepared for the measurement. The flow controller is completely closed, the injection volume is brought to a rather high pressure of the processing gas. The collection volume is evacuated and the TMP is kept running at all times.
Then the flow controller is opened to a specified flow value which is noted. The pressure rises preferably to the regime where RP301 is operational and its value is noted. Otherwise the flow value or the pressure in the injection buffer must be increased. Readings for different flow values and gases are taken.

Calibration

First the values of the flow controller are corrected by the calibrations worked out ahead (see section 4.3.2.1). The pump speed is determined by plotting the real gas flow (Q_{real}) against the pressure reading of RP301 which is considered the true pressure (p) inside the system.
A linear fit yields the slope which is identical with the pumping speed (S).

The pumping speeds found at the center of the six-cross are

N_2	$S = 33.1\text{l/s}$
Ar	$S = 29.2\text{l/s}$
He	$S = 37.7\text{l/s}$
Ne	$S = 30.3\text{l/s}$

4.3.2.3 Determination of low pressures

The result for the pumping speed can be assumed as independent of pressure as long as one stays in the molecular gas regime. By solving equation 4.8 for the pressure

$$p = \frac{Q}{S} \tag{4.9}$$

the real local pressure inside the system can be evaluated by plugging in the real gas flow and the pumping speed for the respective gas.

Measurement via pressure gradient

The measurement is basically the same as for the determination of pumping speed (section 4.3.2.2) but is exercised at much lower pressures. Instead of RP301 the reading of the cold cathode pressure RP303 is taken.

Calibration

The plot of the fraction Q/S against the read-out values of the cold cathode p_{RP303} is the calibration for the cold cathode.

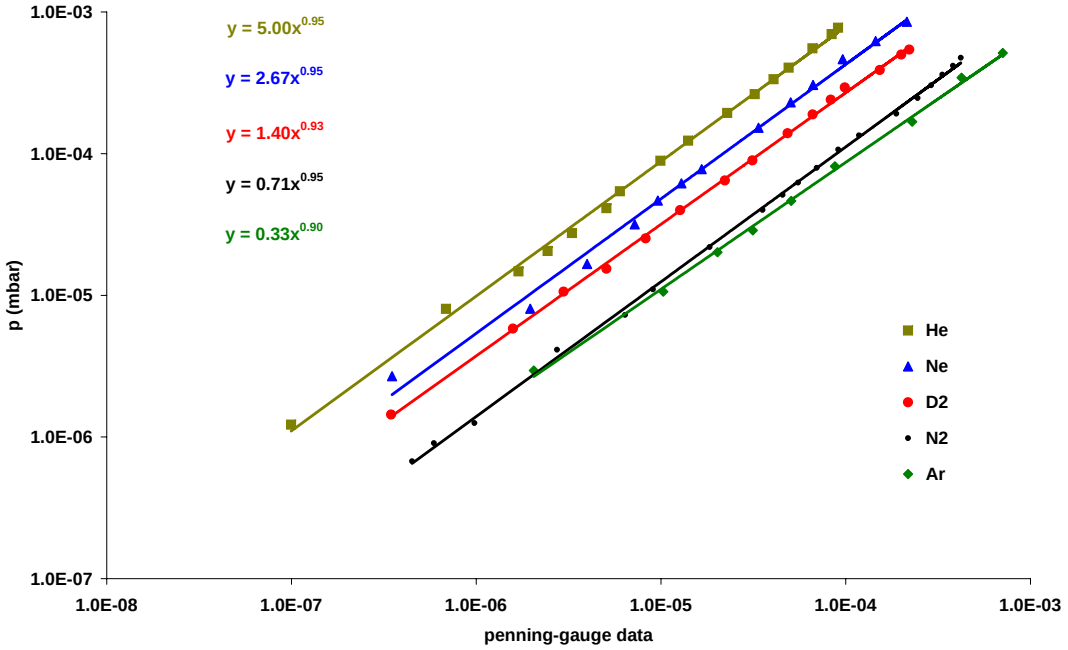

Figure 4.4: **Calibration curves for the cold cathode pressure gauge RP303 for different gases.** The data is fitted by linear functions for each gas type.

A potential fit was done to the data that lay in the confidence regime between 10^{-7} and 10^{-3} mbar. The yielded results are:

He	$p = 5.00 \cdot (p_{\mathrm{RP303}})^{0.95}$
Ne	$p = 2.67 \cdot (p_{\mathrm{RP303}})^{0.95}$
Ar	$p = 0.33 \cdot (p_{\mathrm{RP303}})^{0.90}$
N_2	$p = 0.71 \cdot (p_{\mathrm{RP303}})^{0.95}$
D_2	$p = 1.40 \cdot (p_{\mathrm{RP303}})^{0.93}$

4.3.2.4 Time extrapolation to lower pressures

Another possibility to calibrate the cold cathode to lower pressures is to take the pressure rise technique from section 4.3.2.1. One extrapolates the reading of RP301 to earlier times, assuming the linearity of gas flow over broad pressure ranges, and compares it to the readings of RP303. This method can but return false results if the assumption of linearity is not correct or deviated at some point. Nor can it help to access lower ranges below the initial pressure the measurement started from. It was therefore at best used as complementary.

4.3.3 RGA calibration

A calibration of the RGA mass analyzer (Pfeifer QMS 200 Prisma) is needed as well. It should later be possible to determine the partial pressure of a processing gas inside the collection volume by taking a mass spectrum and a quick inspection for prominent peaks.

RGA operation

Residual gas analysis (RGA) is a technique to analyze gas for its composition of different gas species and is an application of mass spectroscopy. The operational device, called residual gas analyzer (RGA), in general consists of three major assembly parts: an ion source, a mass spectrometer and an ion detector.

The work principle is as follows: The molecules of the gas being analyzed are turned into ions through electron impact ionization. For this an electron beam generated by a hot emission filament and extracted by means of an electric field is used. The filament is but easily destroyed by reactive gases like oxygen and their increased abundance at high pressures. This limits the RGA's application to pressures lower then 10^{-4} mbar. The ion beam is then analyzed by a radio frequency quadrupole system: AC and DC currents are applied to 4 concentrical rods. Only ions with a matching eigenfrequency which is determined by their charge-to-mass ratio are allowed to traverse inside the quadrupole, all other ions are kicked out. Behind the quadrupole rods lies a sensitive ion detector.

RGA mass spectra are usually represented as a chart with the mass-to-charge ratio on the x-axis and the relative intensity on the y-axis (see figure 4.5). The peaks exhibited by a mass spectrum need to be interpreted properly since these can be ambiguous in certain cases, such as when two different molecules exhibit the same mass. Knowledge of how two different molecules with the same mass would dissociate into smaller fragments of different mass-to-charge ratios (known as cracking patterns) allows an absolute identification of the gas species.

Measurement

The RGA is connected to a computer running the necessary software "*Quadstar-32bit*". The software is operatated as stated in [PfeQS] and [Luk08c].

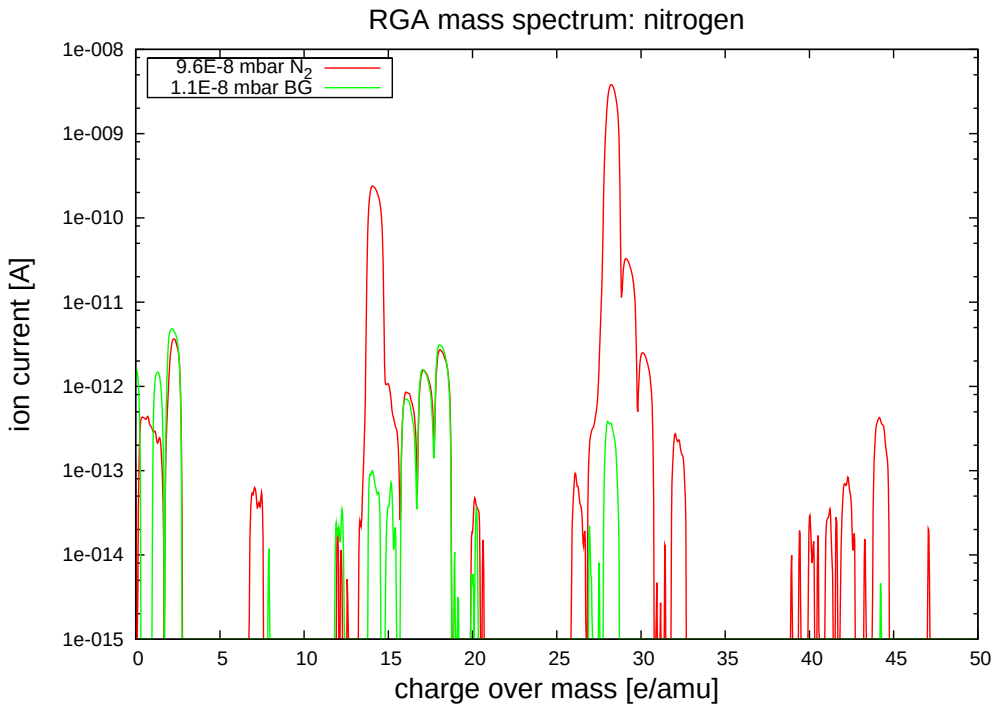

Figure 4.5: **Mass spectrum of nitrogen atmosphere.** Shown is the ion current against the charge-to-mass ratio recorded by the RGA301. Curves for $9.6 \cdot 10^{-6}$ mbar nitrogen and the background are plotted. The elevation of specific peaks known from the cracking patterns, here at 14, 28, 29, 30, identifies the nitrogen and allows the calculation of its partial pressure.

Before any measurement the setup is evacuated, especially the collection volume. The end pressure in the collection volume is noted and an RGA background spectrum is taken by the procedure above. Then the collection volume is injected with the processing gas. This can be done by a constant pressure or a pressure gradient. Either way the pressure gauge RP303 must state a stable pressure and must be in the allowed RGA operation regime below 10^{-4} mbar. Only then is the pressure reading being noted.
The RGA301 is activated subsequently and a mass spectrum recorded and saved. The name of the saved files was chosen in a way they could be easily recognized and itentified in the various data sets. The scheme was "*gastype_date_time_pressure.filetype*".
The calibration measurements were repeated with different pressures and gases to gain enough statistics for a calibration set of each gas.

Data processing

Before the calibration can be accomplished the data must be prepared and processed by different tools to extract the information needed.
As a first step the saved mass spectra are converted from the "*.sac*"-format into a

plain readable ".txt" upon opening them in the provided program "*dispsav.exe*". The "*.txt*"-files can later be easily imported into any spreadsheet-calculation program.

As each spectrum is accompanied by a lot of data values, the relevant information is saved to a new file that is given the name "*peak map*".

The first step is the indexing of the spectrum for different prominent peaks according to the cracking patterns of the analyzing gas. These cracking patterns express how gases break up into smaller fragments when they are ionized and what their relative abundance is. They are based upon chemical and isotopic properties of the gas. Table 4.2 states these cracking patterns for the processing gases involved at the experiment. The ion current to each of this prominent peaks (I_{peak}) is noted in the peak map.

As second step the program "*MAFI*" by Florian Fränkle [Fra08] is used to extract the abundance of up to eight different gas types from the spectra. This is done by a fit of the original spectrum to the cracking pattern of Ar, CO_2, CO, H_2, N_2, O_2, H_2O and the respective processing gas. An additional parameter to this computation is the ionization probability of each gas that must also be provided to the program. Table 4.3 states these probabilities for the processed gases. The program returns the best fit and the computed perceptual abundance (f) of each gas, also noted to the peak map.

At last the peak map is completed by the recorded pressure reading of RP303 which is corrected to the real pressure (p_{real}) by calibration (see section 4.3.2.3).

Table 4.2: **Cracking patterns of processing gases.** [Ley02] Position and relative hight for processing gases nitrogen, argon, deuterium, helium and neon

Name	Position [e/amu]	Composition	rel. hight
Peak(28)	28	$^{14}N_2^+$	100%
Peak(14)	14	$^{14}N_2^{++}$	7%
Peak(29)	29	$(^{14}N\text{-}^{15}N)^+$	1%
Peak(30)	30	$^{15}N_2^+$	<1%
Peak(40)	40	$^{40}Ar^+$	100%
Peak(20)	20	$^{40}Ar^{++}$	20%
Peak(36)	36	$^{36}Ar^+$	0.3%
Peak(38)	38	$^{38}Ar^+$	<0.1%
Peak(18)	18	$^{36}Ar^{++}$	<0.1%
Peak(4)	4	$^{2}D_2^+$	100%
Peak(2)	2	$^{2}D^+$	1%
Peak(4)	4	$^{4}He^+$	100%
Peak(20)	20	$^{20}Ne^+$	100%
Peak(22)	22	$^{22}Ne^+$	1%
Peak(21)	21	$^{21}Ne^+$	0.3%

Table 4.3: **Ionization probability of different gases.** [Ley02] Relative ionization probability of vacuum relevant and processing gases; nitrogen is defined as unity

Gas	rel. IonP
CO_2	1.4
CO	1.05
H_2	0.44
O_2	1.0
H_2O	1.0
Ar	1.2
N_2	1.0
He	0.15
Ne	0.23
D_2	0.35

Calibration

The completed peak map now contains all the data necessary for the calibration.
The calibration set for each gas is gained by plotting the partial pressure ($f \cdot p_{\mathrm{real}}$) against the ion current of the dominant peak (I_{peak}). It is advisable to use the dominant peak, as it elevates highest above the background level. Only if the same charge-to-mass ratio is occupied by another gas fragment one should shun to the next leading peak.

The obtained data is plotted in figure 4.6. No closed fit function could be found describing the whole pressure range of each gas. So up to three broken potential functions were fitted instead, as stated in table 4.4.

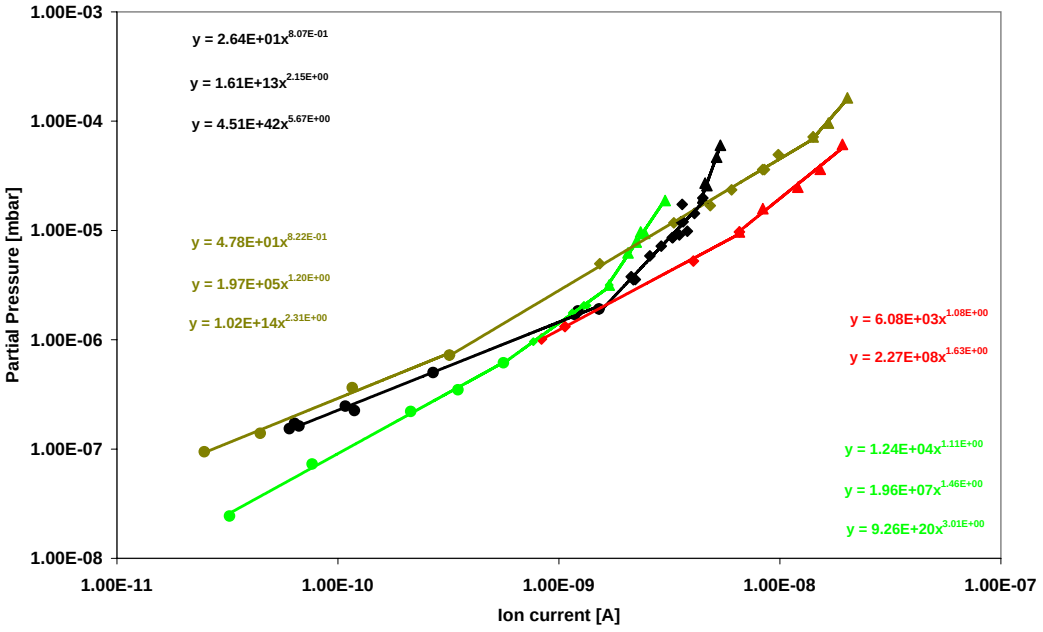

Figure 4.6: **Calibration of the RGA for different gases.** Identification of the partial gas pressure by the measured ion current of the associated dominent peak. Also shown are broken fit functions to the data. Black N_2 peak 28, Brown He peak 4, Green Ar peak 40, Red D_2 peak 4.

Table 4.4: **Calibration of the RGA.** Stated are the peak investigated and the gas being associated. The second and the last column state the scope of each calibration function, in the third column computed the partial pressure is listed.

Gas	I_{lower} [A]	p_{part} [mbar]	I_{upper} [A]
N_2 peak 28	$6.4 \cdot 10^{-11}$	$2.64 \cdot 10^{1} x^{0.807}$	$1.5 \cdot 10^{-9}$
N_2 peak 28	$1.5 \cdot 10^{-9}$	$1.61 \cdot 10^{13} x^{2.18}$	$4.5 \cdot 10^{-9}$
N_2 peak 28	$4.5 \cdot 10^{-9}$	$4.51 \cdot 10^{42} x^{5.67}$	$5.3 \cdot 10^{-9}$
He peak 4	$2.9 \cdot 10^{-11}$	$4.78 \cdot 10^{1} x^{0.822}$	$3.2 \cdot 10^{-10}$
He peak 4	$3.2 \cdot 10^{-10}$	$1.97 \cdot 10^{5} x^{0.81}$	$1.4 \cdot 10^{-8}$
He peak 4	$1.4 \cdot 10^{-8}$	$1.02 \cdot 10^{14} x^{0.81}$	$2.2 \cdot 10^{-8}$
Ar peak 40	$2.9 \cdot 10^{-11}$	$1.24 \cdot 10^{4} x^{1.11}$	$5.6 \cdot 10^{-10}$
Ar peak 40	$5.6 \cdot 10^{-10}$	$1.96 \cdot 10^{7} x^{1.46}$	$1.6 \cdot 10^{-9}$
Ar peak 40	$1.6 \cdot 10^{-9}$	$9.26 \cdot 10^{20} x^{3.01}$	$3.0 \cdot 10^{-9}$
D_2 peak 4	$8.3 \cdot 10^{-10}$	$6.08 \cdot 10^{3} x^{1.08}$	$6.5 \cdot 10^{-9}$
D_2 peak 4	$6.5 \cdot 10^{-9}$	$2.27 \cdot 10^{8} x^{1.6}$	$1.9 \cdot 10^{-8}$

4.3.4 Gas release properties during cryo pump warm-up

After the measurment devices relevant to the experiment have been successfully calibrated, the investigation of the gas release properties of the cryopump has to start. These have been performed and discribed in [Luk09a].
It was found that a release fraction of deuterium that was once captured on the cryopump of $(83 \pm 3.4)\%$ can be achieved by allowing a slow warm-up of the pump to 120 K. Unwanted background of other gases, however, can be supressed as long as the release temperature is kept below 140 K.

4.4 Additional corrections

Besides the necessary calibrations must one also account for corrections that result from the experimental substitution of the CPS by the collection system and the use of deuterium as stated in [Luk08a] and [Luk09a].
The different performance of the CPS and the collection system can be expressed by their respective capture factor. Investigations in this regime showed that the collection system achieves a reduction factor for deuterium of approximately 1.5%. The CPS is expected to capture up to 2.26%, as calculated with the transmission matrix estabilshed by X. Luoa[Luo05]. This means a correction factor of 0.76 must be included in the experiment's calculus.
Also one must account for the different performance of the DPS2-F module for deuterium instead of tritium: The lighter deuterium is harder to be pumped. This can be accounted for by a additional factor of 2 to the reduction factor obtained for deuterium.

4.5 Preliminary tests with leak detector

When the calibration measurements with the reduction factor facility had already begun Klaus Schlösser (IK) stated that a live measurement of the gas flow at the exit of the DPS2-F might be possible with the use of a helium leak detector. This device fulfills two key demands: It already has an integrated valuation and background suppression mechanism in form of a mass spectrometer and can measure very tiny flows. The spectrometer is preset for the mass of atomic helium (^{4}He) which is exactly the same as for molecular deuterium (D_2). They but differ in their ionization probability why a correction of factor 2.93 is needed.
Preliminary tests of the leak detector (Adixen ASM 142D) together with the injection system showed that the gas flow value can be measured by the leak detector with $30 - 50\,\%$ deviation [Schl09]. This is not precise enough for use in the reduction factor measurement but a valid method to quickly perform a check of the gas flow at the DPS2-F's output.

4.6 Results and conclusion

The calibration phase of the reduction factor test measurement at the DPS2-F has successfully been concluded.
The experimental setup consists of 2 systems that get connected to the DPS2-F module:

An injection and a collection system. Deuterium, but also helium, neon and argon are used as processing gases. By comparison between the gas flow that is injected into the DPS2-F and the remaining gas flow at its exit the reduction factor will be determined. Necessary calibration tasks have been carried out: The volumes of the setup have been determined, the flow controller RV201 and the pressure gauge RP303 were successfully calibrated. Subsequently, a calibration of the RGA has been worked out that distinctly returns the partial pressures of the processing gas. Also other important properties concerning the measurement have been investigated.
Thereby the injection system is able to provide a stable gas flow with approximately 2% precision. By measurement with the collection volume the gas flow at the exit can be determined within runtimes of approximately two days. All results are well documented and safety guidelines are worked out so that the setup is ready for its application at the DPS2-F.

5. Contributions to the development of new test ion sources

This chapter focuses on the development and testing of ion sources at KATRIN and discribes ion sources of two generations and their utilization for the plasma test measurements performed at the source and transport section. At first the purpose and work principle are outlined in the context of the proof-of-concept ion source ELIOTT. During this thesis it was further developed into the present second generation ion source ELIOTT 2. The changes introduced and the improvements are pointed out. These were evaluated and the source was characterized by measurements performed at the MPI-K, Heidelberg. The chapter will conclude with suggestions and ideas for a final generation ion source which will find application at the test measurements of DPS2-F.

5.1 Purpose and work principle

5.1.1 Requirement on an ion source

As described previously in section 3.5, tritium ions from the initial β-decay in the WGTS, but also ions from secondary reactions, pose a serious threat to the proper measurement of the neutrino mass. These unwanted ions must by all means be removed from the beam and their density inside the spectrometers must be kept as low as possible. That is the task of the transport section. Its capability of removing ions must be tested and probed before KATRIN goes into operation. Otherwise one would risk the contamination of the setup by tritium ions that were not successfully removed.
For these so called test measurement the transport section must be exposed to the same or a similar ion plasma as it is created by the WGTS:

- gas flow of $Q \approx 10^{-2}\,\frac{\text{mbar}\cdot\text{l}}{\text{s}}$
- pressure $p \approx 10^{-5}\,\text{mbar}$
- magnetic field of $B = 5.6\,\text{T}$ (entrance of DPS2-F)
- ion current of $A \approx 100\,\text{nA}$, uniformly distributed over the whole magnetic flux tube cross-section
- same ion species as created by the WGTS

A major concern is how to substitute the radioactive tritium by a safe processing gas without losing its unique properties concerning gas kinetics, electronic and chemical

behavior.

Correspondingly a device had to be indentified that could create this ion plasma under safe and sound working conditions: An ion source.
The investigations in this field led to the founding of the ion source project and were first handled by Michael Schöppner during his diploma thesis [Scho08].

One of the first points that needed clarification was the processing gas to use. It was settled for the lighter hydrogen isotope deuterium. As isotopes, deuterium and tritium share almost the same electric properties. The chemical behavior in all important aspects is also the same. The missing neutron has but a massive impact on the involved kinetics because the charge-to-mass ratio (q/m) for deuterium is increased by 50%.
The next step was the investigation on how the deuterium gas should be ionized. Different methods were considered. Electron impact ionization proved the best option concerning a reasonable high ion production in the rather strict boundary conditions at KATRIN.

The following steps were the development and design of a setup which unifies the work premises and conditions required. This involved the inclusion of following aspects:

1. a similar type of setup is to be installed at the transport section
2. a setup that meets the high vacuum and cleanness conditions at KATRIN
3. an inlet device for deuterium and other processing gases
4. a mechanism to create slow and uniformly distributed electrons
5. a mechanism to accelerate the electrons to make them eligible for electron impact ionization
6. a mechanism to separate electrons from the created ions
7. a mechanism to confine electrons and ions, so that the currents can be guided in a desired (forward) direction

All these points influenced the development of the first test design that later on would become the proof-of-concept ion source ELIOTT. In the next section this peculiar ion source will be discussed. At this point only the very heart of this setup, the ion production chamber is described and its physical principles are outlined.

5.1.2 Work principle

At first, a suitable solution for the physical mechanisms involved had to be investigated, before dimension and design issues could become of any concern. Of special interest is the point of how to create the electrons that later on will be needed for the electron impact ionization. It was deduced that the photoelectrical effect can ideally be utilized.

It creates electrons from an irradiated cathode surface with a number density and velocity, which can be precisely controlled by the intensity and wavelength of the light. Use of this effect is also preferred if taking into account the magnetic conditions in DPS2-F which houses a very strong magnetic field, which limits charged particles to very narrow cyclotron motion. This means that in order to archive an uniform distribution of electrons over the whole cross-section of the beam tube, the electrons must already be created on the very same magnetic field line where they are required later on in the application process. The photoelectrical effect can provide this because electrons are equally agitated over the whole irradiated area of the cathode surface.
After their creation the rather slow electrons have to be accelerated to make them eligible for impact ionization. This is achieved by an applied electric gradient. The kinetic energy of the accelerated electrons should be of the order of $50 - 60\,\mathrm{eV}$ so that they have the maximal cross-section for impact ionization [IonOL]. The actual ionization process at residual gas atoms of the desired gas type can then take place creating a cold plasma. The plasma contains ions, slowed down primary and secondary electrons from the impact, but also fast primary electrons which did not collide. The plasma must then be fast purified from the negative charged electrons in order to keep the recombination rate low. This can be achieved by positive charged electrodes. The presence of the magnetic field positively influences the last mentioned mechanics. The confinement to cyclotron motion prohibits the plasma to diffuse and thereby its disintegration at the outer walls.

These arguments stress that the key for the successful experiment is a clever installment of electrodes. The following sketch in figure 5.1 illustrates how the mechanisms described above are put to work.
The photocathode on the left side is radiated by high intensity UV-light causing the agitation of electrons by the photoelectrical effect. A negative applied voltage helps the electrons to escape. In the next stage a positive voltage at the accelerator electrode increases the electrons' kinetic energy and makes them eligible for electron impact ionization. Some electrons collide with residual gas atoms in the region of the now following cylinder electrode which is also on positive voltage. This attracts primary and secondary electrons from the created plasma and thereby removes them while positive ions are hindered by electrostatic repulsion to diffuse to the outer walls. The positive potential also increases the gradient wall that secondary electrons have to run up against in forward direction, when they face the negative charged extractor electrode. Its potential slightly exceeds the kinetic potential of the fastest (uncollided) primary electrons. By this measure almost all electrons are reflected back to the cylinder region where they may again cause ionization reactions. The positively charged ions on the contrary are attracted by the extractor electrode and will stream in forward direction. So it is thus possible to create a rather pure beam of ions whose density and velocity can be controlled by parameters applied at the electrode setup.

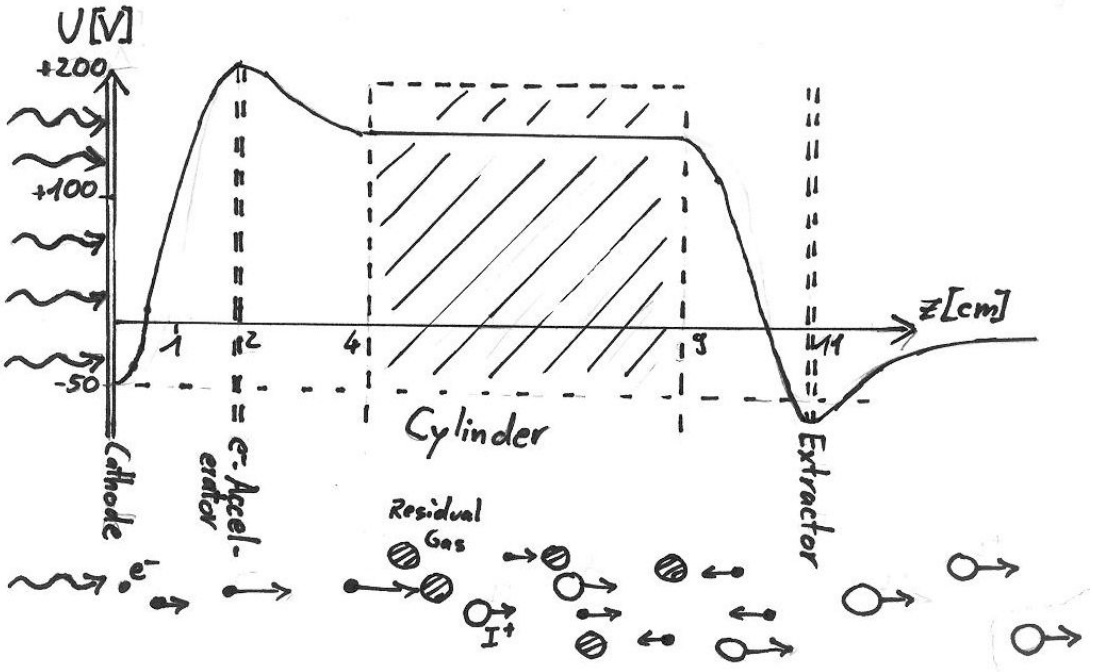

Figure 5.1: **Illustration of the designated work mechanism of the electrode setup.** The top shows the dimensions of the electrode installment and the electric potential that is applied there. On the bottom the action on the particle level is sketched.

5.2 Proof-of-concept ion source ELIOTT 1

The basic principle had to be put to work in a first proof-of-concept ion source. It was given the name of ELIOTT[1] (1). The hole setup was designed and built in the framework of the diploma thesis of Michael Schöppner [Scho08]. The setup was situated at the pre-spectrometer hall at the FZK.

ELIOTT 1 had the following objectives:

- test if the desired ion creation mechanism works
- provide similar test conditions as present at the entrance of DPS2-F (pressure, presence of magnetic field)
- provide the possibility to test the setup with different gas types
- if it should work, provide information and suggestions for improvement for future ion sources (how can the achieved ion current be maximized?)

The electrical setup was manufactured as stated above and shown in figure 5.2. The cathode consisted of a front-lit (reflection mode) copper plate, the other electrodes were made of stainless steel metal grids. The electrodes were mounted onto a vacuum flange which also provided a Swagelok gas connection.
The test setup, as shown in fig 5.3, was made up around a linear vacuum tube where the electrode setup was inserted in by front. On the opposite side, a Faraday cup was situated to pick up the currents. The vacuum tube was also equipped with access ports for vacuum gauges and pumps. A hand manufactured electro-magnet wrapped around the vacuum tube providing the 146 mT guiding magnet field.
The whole mock-up of ELIOTT was finished in the beginning of 2008 and the properties of the ion source ELIOTT were tested.

[1] **EL**ectron impact **Io**n source to **T**est the **T**ransportsection

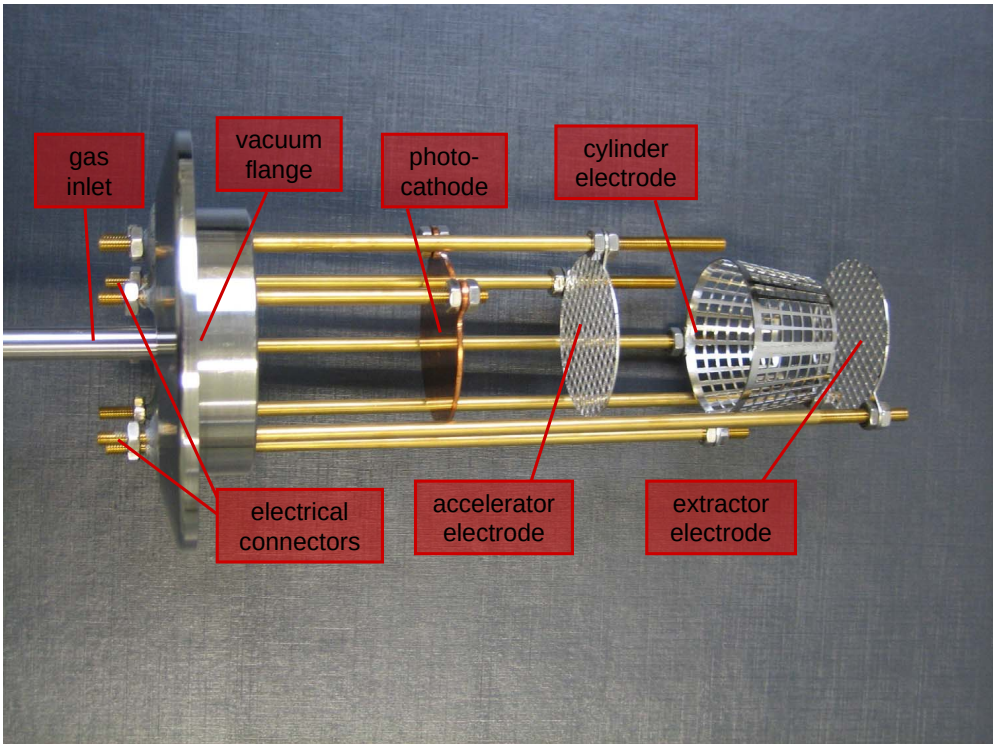

Figure 5.2: **Electrode setup of ELIOTT.**

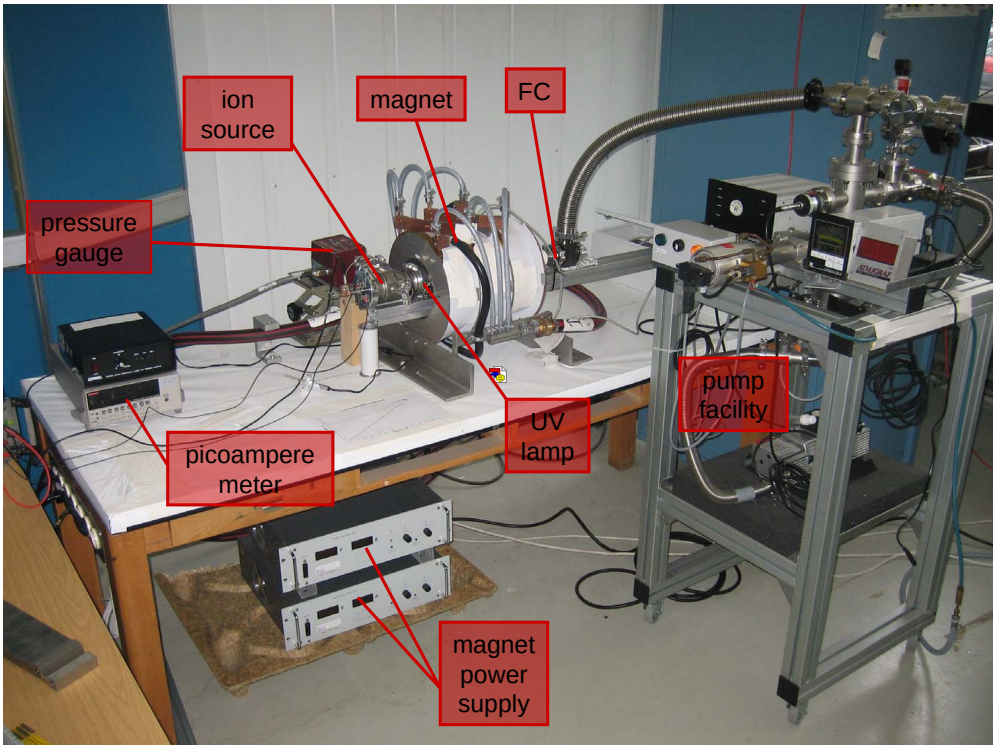

Figure 5.3: **Experiment facility of ELIOTT.**

In fact ELIOTT operated as intended and reasonable ion currents were achieved. The best results where returned for the following configuration (under stable and safe running conditions):

- pressure 10^{-3} mbar of deuterium (front pressure gauge)
- electrode voltages of photocathode +5 V, accelerator +25 V, cylinder +200 V and extractor +60 V
- maximal magnetic field of 145 mT

The maximum yielded ion current at the Faraday cup was 12 nA. A repeated measurement one year later confirmed the findings and amended them where necessary [Zol09a] (see figures 5.4 and 5.5). Therefore the proof-of-concept ion source ELIOTT was a great success!

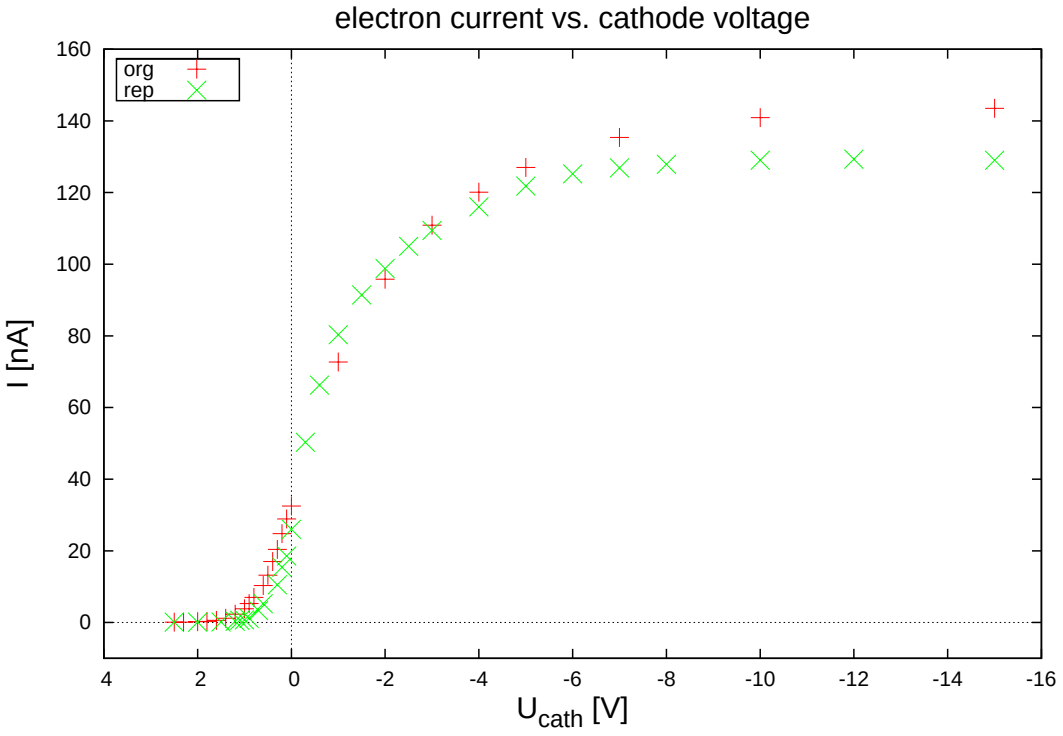

Figure 5.4: **Measurement of ELIOTT 1 electron current against the photocathode voltage at 10^{-6} mbar.** The diagram shows the original (org) and repeated (rep) measurement.

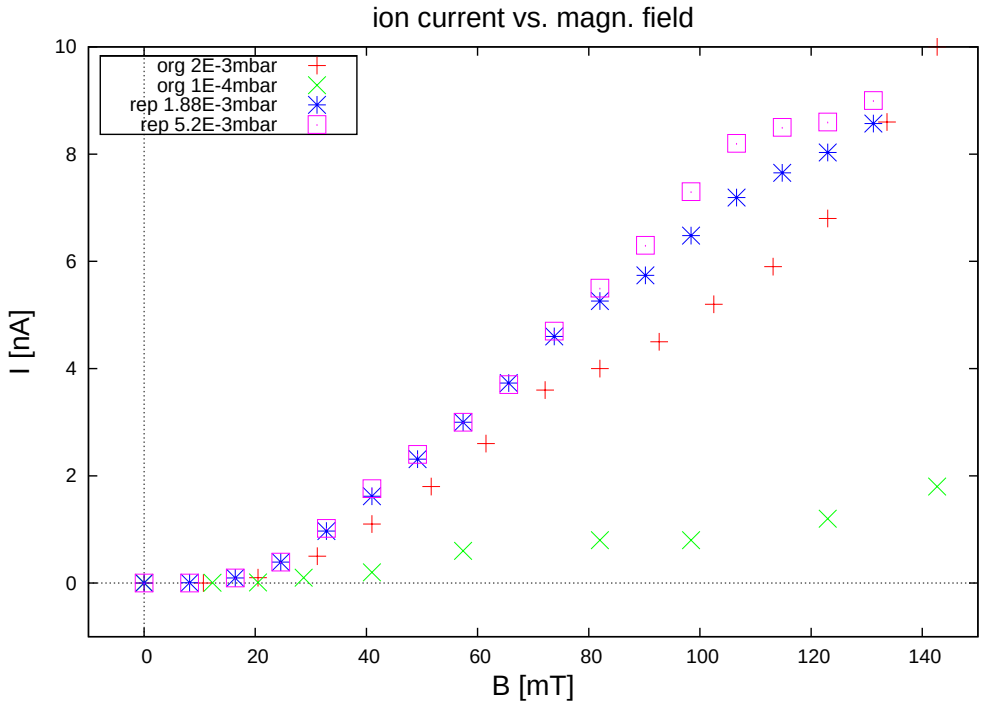

Figure 5.5: **Measurements of ELIOTT (1) ion current against the magnetic field for different pressures.** The diagram shows the original (org) and repeated (rep) measurement.

However, ELIOTT yielded some problems and issues not foreseen:

- The magnetic field strength was limited to 146 mT, while the ion current still rises with the magnetic field and yet shows no saturation. The ion current might be further increased if the magnetic field is likewise. This, however, is prevented by the limited cooling capability and power supplies.
- Computer simulations by Ferenc Glück [Glu08] showed that the magnetic field is not quite as homogeneous as required: in fact it is bulging. This means that electrons and ions created have to run against an increasing magnetic gradient. If the gradient is steep and the particles' starting angle is distributed disadvantageously, particles are reflected, a effect known as magnetic mirroring.
  This means that a fraction of electrons and ions is lost along the way to the Faraday cup and is not being registered there.
- While stainless steel has a lower work function than copper, the latter has proven a better cathode material, as it produces 30 times more photo electrons. It is still unknown why.
- The light beam of the UV-light source did not only irradiate the front-lit photocathode but also the vacuum tube walls and other electrical parts (by reflections). This means that by the bad focusing a lot of the original light intensity is lost. Also disturbing effects are induced by the stray UV-light.

To dealing with these issues was a major task of the next generation ion source.

5.3 The next generation ion source ELIOTT 2

After ELIOTT had demonstrated the feasibility of the electron-impact ion source concept the development of the FT-ICR traps (see section 3.1.3) at the MPI-K had proceeded to a point, where one already had to thing about how the device could be tested and calibrated. So in a joint operation a new ion source was developed especially for the needs of the FT-ICR installment, its name being "FT-ICR test - ion source", or by short ELIOTT 2. It was inspired by the concept of ELIOTT (1). Its development started in the first quarter of the year 2008 and the setup was ready assembled in November 2008 and underlies improvement until now.

This section states the purpose and application of ELIOTT 2. It handles the design and technical issues involved by pointing out changes and improvements made in regard to ELIOTT (1). Also it presents its performance and results in test and characterization measurements. It concludes with discussions and suggestions for improvements of future generation ion sources.

5.3.1 Changed requirements on ELIOTT 2

The new design of ELIOTT 2 had to deal with two important issues: a solution to the problems of ELIOTT (1) had to be found and the new setup had to meet the changed conditions of the FT-ICR installment. These are:

- a produced ion current and density in the range of the FT-ICR trap's detection level (min. 900 ions in the trap's volume)
- operation in a permanent magnetic field of 4.7 T (superconducting magnet)
- dimensions so that it fits in the 110 mm vacuum tube, to which no changes can be done to
- an easy to handle and compact design, so the source can be operated at different places

5.3.2 Changes with regard to ELIOTT 1

The new basic design, as it can be seen in figure 5.6, was influenced most by was the fact that the homogeneous region of the magnetic field at the installment begins not directly at the position of the vacuum tube flange but several centimeters behind it. Also it would not be advisable to insert a UV-light source for front illumination in the vacuum tube, as it was done at ELIOTT (1).
So it was deduced to develop a setup where the cathode can be irradiated from behind (transmissive mode) so that the UV-light source can stay out of vacuum. It is known that such back-lit photo cathodes can be produced by an active very narrow metal layer which is deposited onto a (UV-)transparent material [Jia98]. In this peculiar case, a vacuum window is, acting as the border line between the high vacuum and the atmospheric side where the UV-light source is situated.
In the early development stages it was also found that having the UV-light source exposed to atmosphere and the photons having to travel quite a distance until they reach the cathode plane created some new problems: The gases in air have broad absorption especially in the UV regime (below 190 nm), rapidly decreasing light intensity already at short distances [Pay99]. This problem can but be handled by reducing the number of molecules in the path of the UV-light, for example by pumping. Therefore a solid beam tube must be the connection between the UV-light source and the cathode window accessible for pumping.
The electrode setup stayed essentially the same as the one at the ELIOTT (1) setup, to not introduce too many changes at once which might possibly render the ion source inoperable.

With the basic design laid out the investigation of the individual components could start. Especially the new introduced back-lit photocathode, was of great interest.

5.3.3 Stronger UV-light source

The UV-light source that came to use at the new setup is the model *L10366* of Hamamatsu[HamLS]. It operates by discharges on deuterium and emits in the far UV-regime (160 nm peak wavelength). The source is many times brighter than the one of the ELIOTT (1) setup and focuses in forward direction (approx. 5° light spread). Thus, a distant mounting is possible and a high fraction of the energetic photons will reach the cathode and cause photoagitation.
In addition the lamp is equipped with a vacuum flange which makes the vacuum tight mounting possible, as motivated above.

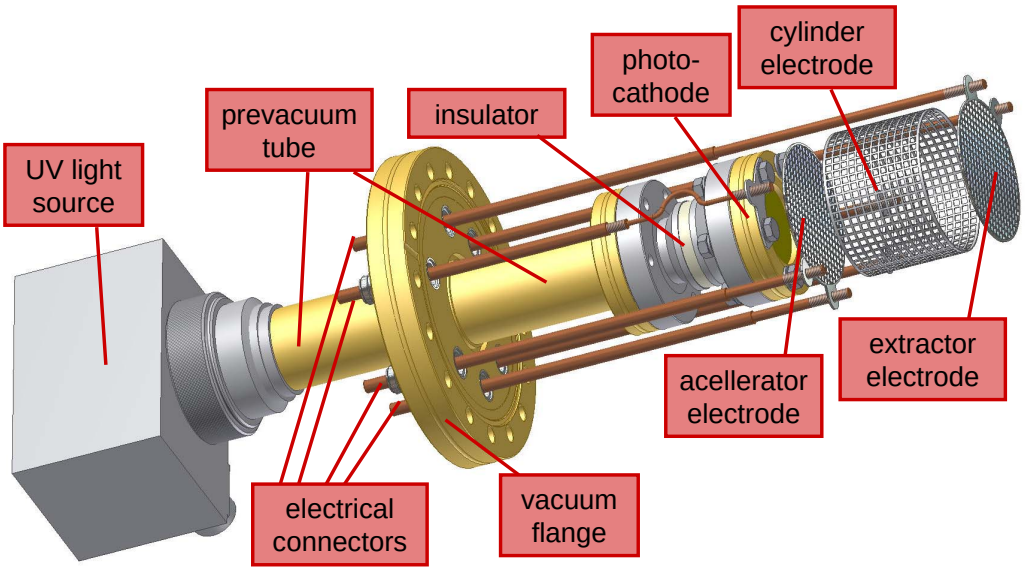

Figure 5.6: **Illustration of the ELIOTT 2 design of March 2008.** The left hand side shows the UV-light source. The beam tube to which it is connected to passes through the vacuum flange and ends at the photocathode window. The active cathode surface is a metal layer which is deposited onto the vacuum window. On the vacuum flange, ceramic insulators are fixing the position of the copper poles which act as fixation and connectors for the electrode setup of accelerator, cylinder and extractor.

5.3.4 Optimization of the cathode window coating

Some effort was invested in the research of how a suitable photocathode window could be manufactured, fulfilling the following demands:

- The window has to be vacuum tight down to pressures of at least 10^{-7} mbar.
- The materials used have to maintain the cleanness of vacuum (low outgasing, low adhesion to surfaces, no adsorption of gas molecules).
- The metal for the active cathode layer must withstand the continuous bombardment by electrons.
- The cathode layer should have a high quantum efficiency with a combined low transmittance of UV-light.

Jiang *et al.* [Jia98] report of excellent properties of cathodes produced by vacuum deposition of a few nanometer thick layer of metal onto a transparent substrate. The material choice was Gold (Au) for the cathode layer. As stated in the paper, it was preferred as it is both anticorrosive and hard to evaporate; it also has a quite high quantum efficiency and broad absorption in the UV regime.
A fused silica 38 mm vacuum window from VACOM was overlayed by gold (20 nm) in MTA[2] at FZK. In order to assure good adhesion of the gold layer, a titanium layer was deposited underneath. The completed cathode window can be seen in figure 5.8.
The thickness of both layers was decided based on the following test.

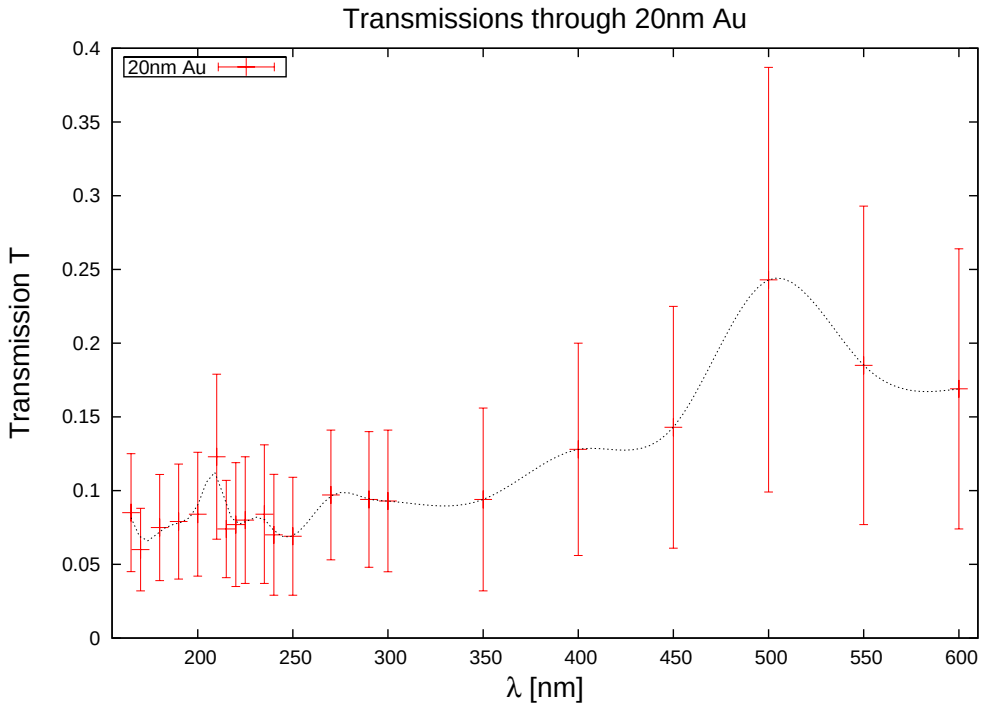

Figure 5.7: **Calculated transmissions for 20 nm Gold.** The graph shows the transmission spectrum as calculated from the spectra obtained at the absorption measurement of the (10Ti+20Au) and (20Ti+20Au) probe carriers. A bold error of 10% on the base data yields the plotted error bars. The connecting line should only guide the eye.

Three small probe carriers were manufactured by the MTA: one consisting of only fused silica ($Si0_2$), like the vacuum window, one additional vacuum deposited with 20 nm Gold and an intersection layer of 10 nm Titanium (10Ti+20Au), and a last one with 20 nm of both Gold and Titanium (20Ti+20Au). They were used in a rough measurement to determine which material combination should be used for the final cathode window coating. For the full report please read [Zol08], figure 5.8 states the

[2] **M**aterial**t**echnische **A**nstalt FZK

calculated transmission for the gold layer.

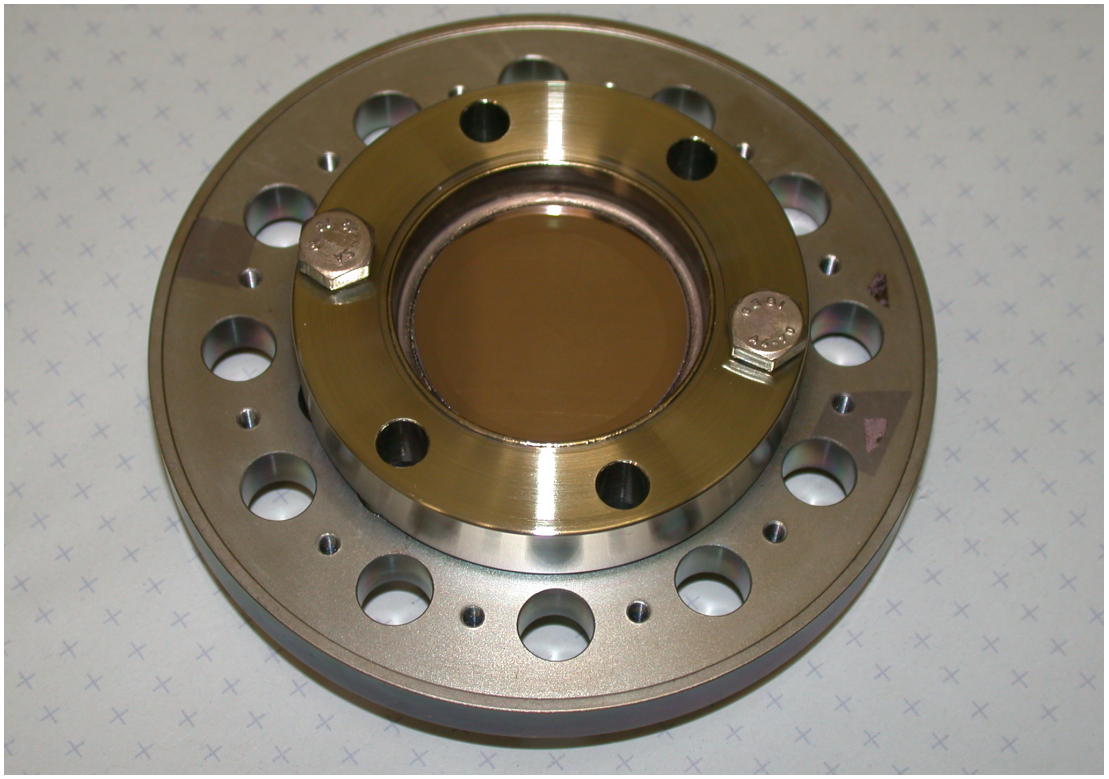

Figure 5.8: **Cathode window of ELIOTT 2.** The manufactured vacuum window with its fused silica plane, which is vacuum deposited by 20 nm Gold and an intersection layer of 20 nm Titanium. Electrical connectivity to the mounting flange is given.

5.3.5 Optimization of the electrode setup

To gain a better understanding about the particle tracks inside the ion source and to optimize the setup computer simulations were conducted. These based upon core algorithms of Ferenc Glück [Glu08] with a newly constructed simulation routine in combination with a newly introduced class object "particle". While the program is working and running in version 1.2.1, the core algorithm had but problems with the computation of particles very close to electrodes. An adaptation of the algorithm was done but could not be implemented until now in the existing code. This subject remains open for further investigation.
(The source code of "trajectory 1.2.1" and further can be provided upon request)

Recently a discussion was initiated on how the electrode plate design might influence the operation of the ion source.
The standard accelerator and extractor electrodes both consist of a narrow metal grid

to generate a homogeneous distribution of the applied potential undisturbed by external space charges. However, the solid grid itself accounts for quite a fraction of the whole covered area posing an impenetrable barrier for particles in flight. Especially in the region close to the symmetry axis where the electron and ion density are maximal a better solution should be found.
A quick simulation showed that the inner 1 cm of the electrode grid could be cut out without distorting the electrode potential too much. Therefore a new electrode of radial design was designed and manufactured in the likeness of a cobweb as illustrated in figure 5.9. The achieved positive effect by the new electrodes must yet be tested.

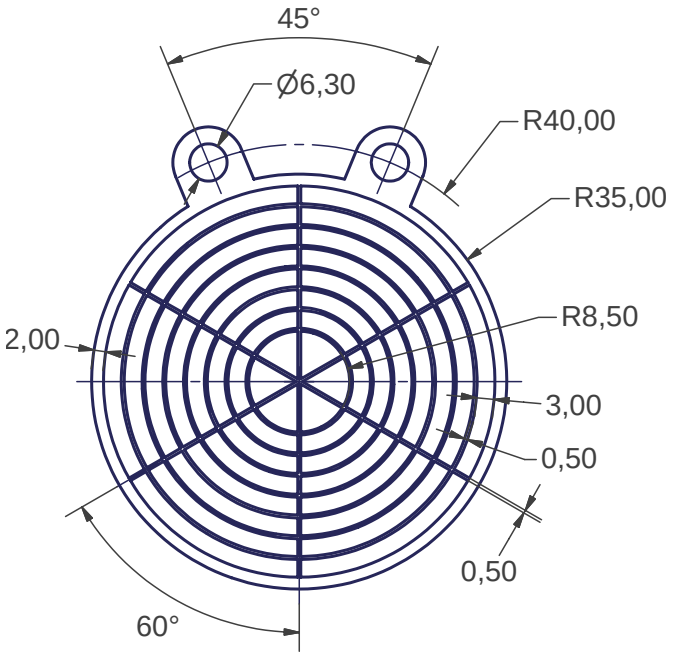

Figure 5.9: **New radial electrode.** The illustration shows the new radial design of the accelerator and extractor electrode. The metal grid consumes less area but still maintains the smooth distribution of the electric potential.

5.3.6 Extension of the source

A later technical solution was that the source might be extended in order to reach deeper inside a magnetic setup. So additional assembly parts for a optional extension of 200 mm were manufactured as it can be seen in figure 5.10.
At the same time a ninsulator ring for the copper poles at the top of the source was introduced. The copper poles were until then subject of torque and deformation whenever the ion source was inserted into the narrow vacuum tube what sometimes resulted in short circuits. The ring makes the electrode setup much more stable and the distances between electrical conducting parts is preserved at all times.
The new dimensions required the electrical poles to be extended. The old copper poles were thus partly replaced by stainless steel onesas the copper-copper screw connection

was often subject of jamming. This problem no longer exists with the new material choice.

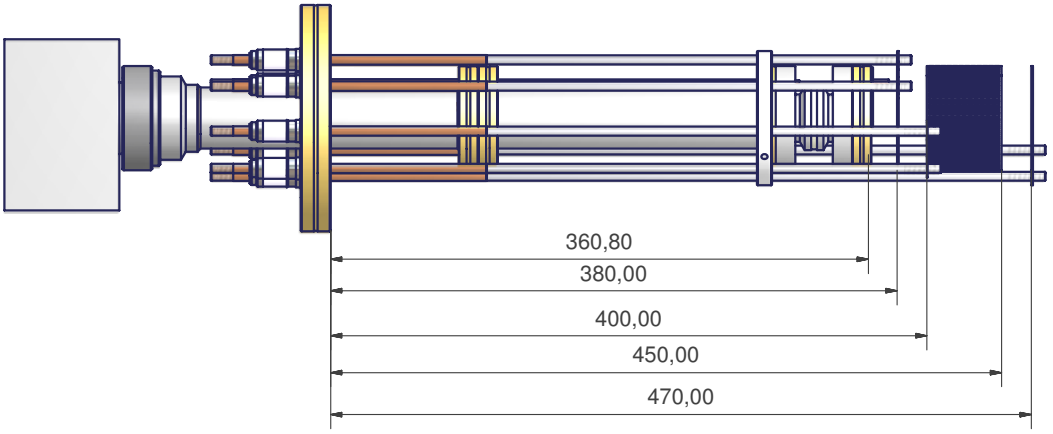

Figure 5.10: **Extended setup of ELIOTT 2.** The illustration shows the 20 cm extension derived from the basic configuration. The setup features an additional beam tube segment, extended steel poles and an electrode stabilization ring at front.

5.3.7 Endplate

An further addition to the setup was an optional possibility to measure the electron and ion current directly at the front of the source by a Faraday cup, called endplate. The endplate is a solid steel metal plate that is fixed onto one of the connector poles of the extractor electrode in the outermost position. The extractor must thereby be shifted a little bit closer to the cylinder electrode which does not disturb the electrical properties too much.
During operation with the endplate basic properties of the ion source can be probed, making the measurement with a distant Faraday cup redundant.

5.4 Test measurements performed with ELIOTT 2

A suitable test setup for the necessary measurements, the one of the FT-ICR tests, was available at the MPI-K in Heidelberg. It provided a 4.7 T superconducting magnet, vacuum tube and the spare vacuum infrastructure.
Different measurements were done to investigate the functionality of the ion source and how it performs under different conditions. At the time of the first measurements in January 2009 the extension of the source was not available yet. The basic version can be seen in figure 5.11.
(For the full detailed report see also [Zol09a])

5.4.1 Setup

Figure 5.12 shows a schematic of the mock-up configuration. For future reference the right hand side is addressed as the front, while the left hand side is addressed as the

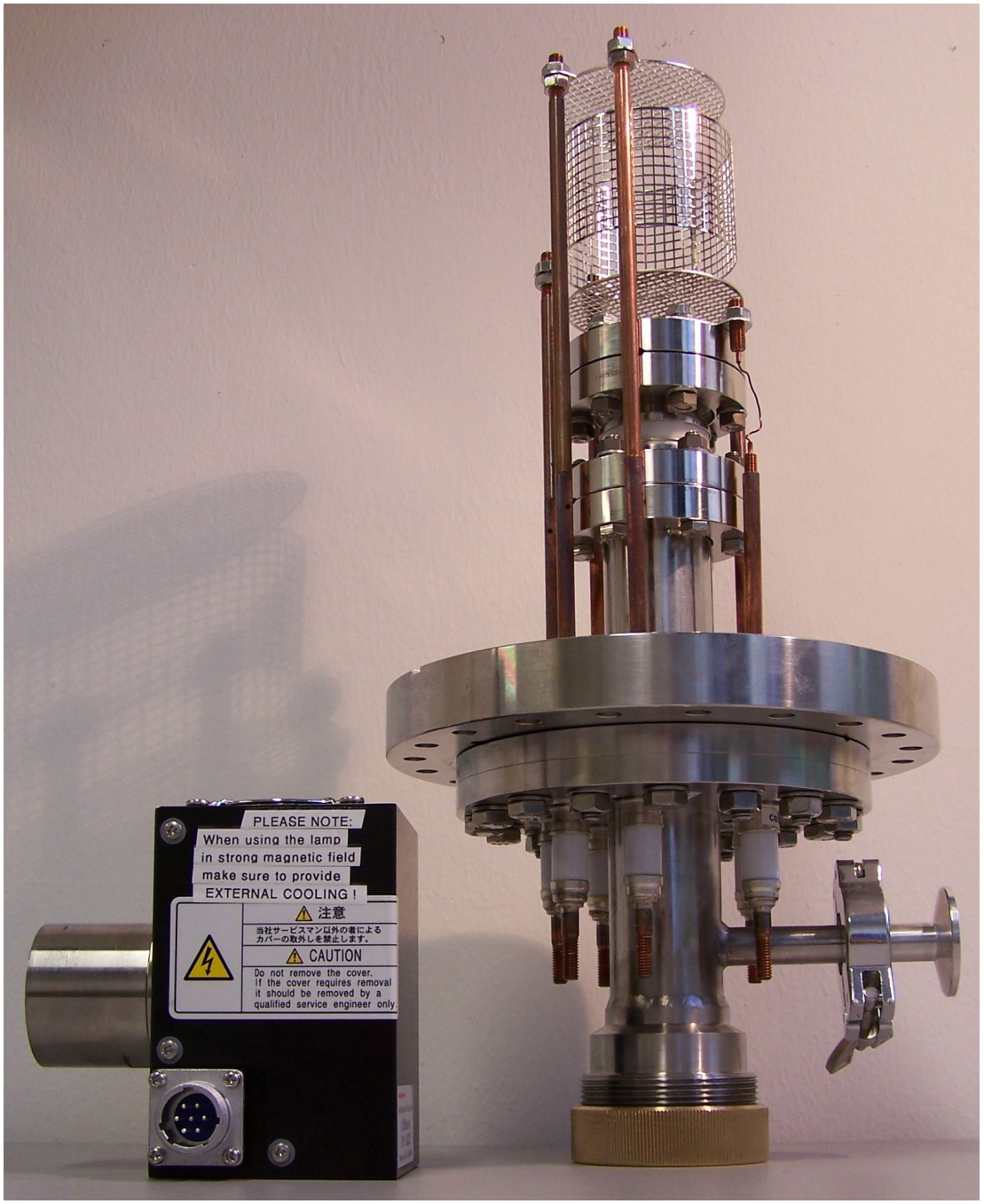

Figure 5.11: **The complete assembled ion source ELIOTT 2 in the basic version.** Shown on the left is the UV-light source. Its vacuum flange (left side) is connected to the ion source at the lock bust ring (right side bottom).

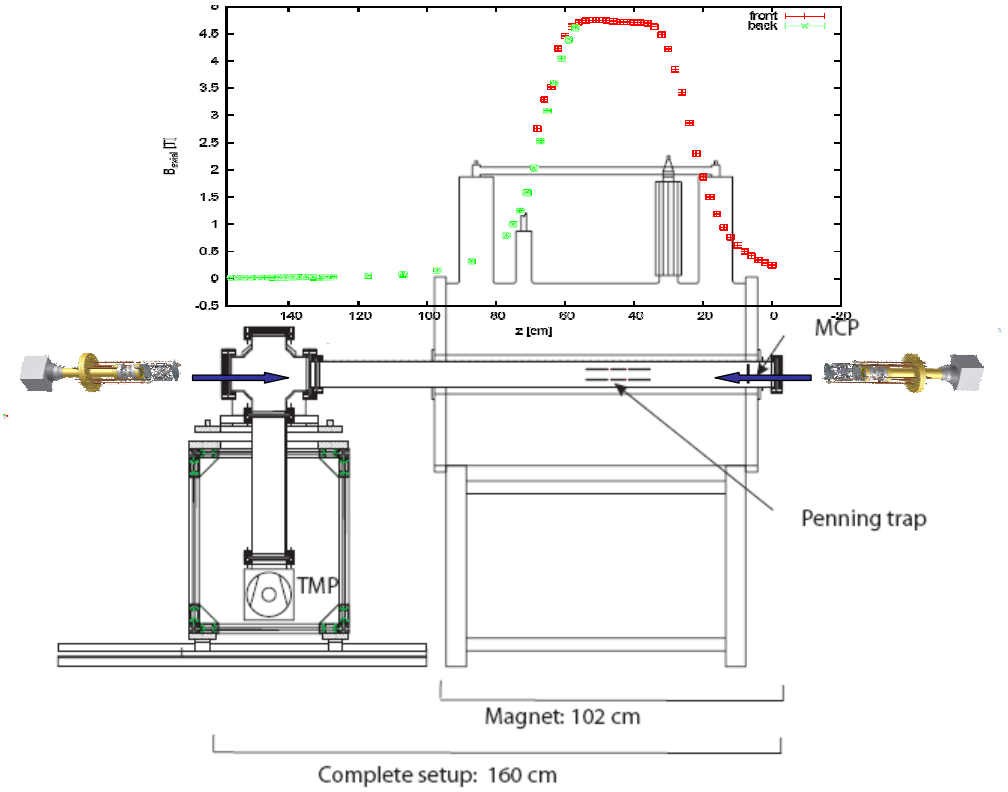

Figure 5.12: **Scheme of the experimental setup at MPI-K**, with magnet, vacuum tube, sixcross, FT-ICR trap and pumps. The ion source is either inserted from the left side (front) or from the right side (rear). The illustration is overlaid by the measured axial magnetic field.

downstream or rear.
The center of the setup is the superconducting magnet of 4.7 T nominal strength with the embedded vacuum tube. At the center the FT-ICR trap is inserted. The front end allows mounting of different devices. On the rear end a sixcross is situated. While its bottom outlet is blocked by the fixed connection to the TMP, the others can be freely equipped with instrumented flanges like pressure gauges, gas inlets or similar. During the measurements the top and the left side flanges were blocked by a pressure gauge and the FT-ICR instrumentation box. This left the right and the front side flange available for mounting.
During the ion production measurements the right side flange was equipped with a gas inlet leading into a small plastic hose which ended at the heads end of the vacuum tube, so that a gas flow and pressure gradient inside the vacuum tube could be established.
The closed off setup can be evacuated by the TMP down to high vacuum pressures ($< 10^{-7}$ mbar).

As additional equipment, a digital operated multi-channel power supply was available. The available detector devices at the setup were

1. the FT-ICR trap with the computer aided signal processing, in a spectral and a species-fixed operation mode
2. a multi-channel plate (MCP)
3. a Faraday cup (FC) with a pre-located metal repulsion grid
4. the endplate described in section 5.3.7

The ion source itself could be mounted from two directions: Either from the heads end side or from the tails end side, in each case facing along the symmetry axis of the vacuum tube.

5.4.2 Initial tests

Some initial tests were performed before and during operation of the ion source. They check the correct assembly and probe basic quantities of the setup and the source. For example the magnetic field is of importance at the ion production process and must therefore be quantified. Along others this enabled a better understanding of the physical processes at work and helped finding positive adjustments to the measurement procedure.

5.4.2.1 Magnetic field

A measurement of the axial magnetic field was thus performed with a Hall probe along the beam axis. The radial field was also probed but was found to be consistent with the axial values inside the boundaries of the vacuum tube.
The results are shown in the diagram 5.13. If this data is overlaid by the geometry of the ion source this results in table 5.1.
It is clearly seen that the rear position houses a very low magnetic field at the position of the ion source. While at the front position the ion source is confronted with a very steep magnetic gradient (2.1 T over 11 cm) at the position of the electrodes.

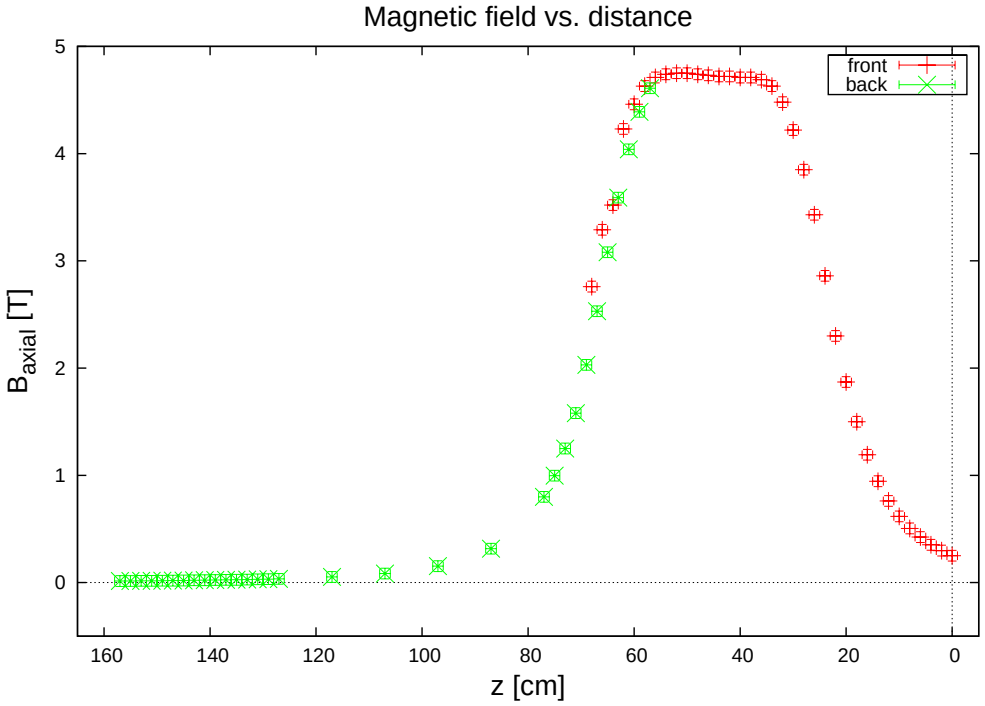

Figure 5.13: **Axial magnetic field along the vacuum tube.** (front flange defined as $z = 0$)

Table 5.1: **Axial magnet field at the ion source**, inserted by front (f) and back (b); additional adapter flange thickness 25 mm

part	pos [cm]	magn.f.(f) [T]	magn.f.(b) [T]
cath	13.5	0.9	0.02
acc	15.5	1.15	0.021
start cyl	17.5	1.43	0.024
end cyl	22.5	2.43	0.026
ext	24.5	3.0	0.028

5.4.2.2 Electrical integrety

Despite the small distance of 2 mm between electrical conducting parts and voltage differences of up to 250 V, no shortcuts could be detected at the ion source at operating pressures.

5.4.2.3 Vacuum tightness

Leakage tests of the ion source showed a leak tightness of the highvacuum side better than 10^{-9} mbar l/s.
If installed and pumped in vacuum setups, the achieved endpressures are quite satisfying. The prevacuum chamber which is connected to the UV-light source by a simple silicone o-ring can achieve endpressures below 10^{-2} mbar by conventional prepumps. This is enough to rarify the UV-absorbing gases so that photons can be transmitted undisturbed.
Achieved end pressures at the high vacuum side were below 10^{-7} mbar using the TMP and a viton seal. This is reasonably low enough to perform tests with the ion source. The designated operation pressures however lie in the region between 10^{-2} to 10^{-4} mbar. These values are forged by the boundary conditions of the DPS2-F, where the ion source must later be applicable. Further benchmark parameters came from the optimum running conditions of ELIOTT 1 which performed best in a $3 \cdot 10^{-3}$ mbar deuterium environment. Pressures below the 10^{-4} mbar level, however, resulted in a massive decrease of ion current as the gas density gets to thin to cause impacts in a significant number.

5.4.2.4 Prevacuum

To get a rough estimate of the improvement in photon transmission by the prevacuum, the photocurrent at the cathode was measured. It showed that the photocurrent has roughly increased by a factor of 6 when the volume was evacuated from atmospheric pressures down to the prepumps endpressure (approx. 10^{-2} mbar).

5.4.2.5 Stability test

To test the stability of the ion source it was mounted onto the sixcross at the rear. An overnight measurement of the ion content inside the FT-ICR was performed. Observed was an exponential decrease by 40% over 8 hours.
Two different explanations arose during the evaluation of the setup: First the pressure reading had decreased from $7 \cdot 10^{-7}$ to $4 \cdot 10^{-7}$ mbar; the rarefaction of the gas making it harder to cause ionization. The second hypothesis favored the observed deposition on the magnesium oxide glass plane of the UV-light source, as a cause reducing the intensity of light transmitted forward to the cathode window. The deposit seemed to consist of a shining metal-like material that had the color of bronze localized at the center of the plane where the UV-radiation is the strongest. The coating could but easily removed by wiping it off.
In later measurements with long runtime of the UV-light source no such deposit was ever witnessed again; its origin still remains unknown.
In all other measurements the source has proven to be stable and no decrease of the initial intensity over long runtime periods was observed.

5.4.3 Measurements

The two possibilities to insert the ion source into the setup differ greatly in the magnetic field (refer to section 5.4.2.1). The front hosts a strong magnetic gradient, while the rear has only a weak field, which does not increase until deep inside the magnet. The work mechanism of the ion source heavily depends on magnetic properties, this is why these two configurations can not be treated as one and the same.

To precisely state experimental configurations, a fast notation was developed. Its from is [U =(*cath, acc, cyl, ext, (endp)*); p = *pres gas*] stating the voltages at *cathode, accelerator, cylinder, extractor* and *optional endplate*, respectively, to the grounded vacuum tube in [V] and the *pressure* and *processing gas* in [mbar]. The comment *var* means that this specific quantity was varied through the measurement.

5.4.3.1 Operation with FT-ICR trap

The ion source was first installed at the rear of the setup where a low magnetic field of only 21 mT is present. It was the first commissioning of the ion source and a good opportunity to test some basic properties and to operate it together with the FT-ICR trap.
The FT-ICR setup was preset on resonant scan for the H_2O-ion signal. Preliminary operation voltages of the electrode system had already been worked out. Nevertheless, these had to be adjusted in a step to step process to find safe running conditions. The UV-light source was switched on and as an initial optimization step the cathode voltage varied. Then followed the accelerator, the cylinder and the extractor voltage.

Diagram 5.14 shows the results for the variation of the cathode voltage. The FT-ICR trap saw this as the "first ions created by the ion source". The observed behavior is the one expected for electron emission of any photocathode: The signal drops to zero if the voltage positively exceeds the difference of photon energy and work function. It rises to zero voltage and continues to rise to negative voltages as charge repulsion helps electrons to escape the cathode region. At a certain point saturation of the signal begins, the maximum quantum efficiency of the material has been reached. This behavior of the ion current, resembling electron emission, can be explained by the coupled creation mechanism of ions by electron impact ionization.
At the negative voltage of -50 V, the ion current is already well in saturation which satisfies the need of a best possible electron current. This voltage is also low enough so that the safe operation of the ion source is still given. It was therefore picked as a preliminary standard parameter value.

As the next point the accelerator voltage was varied. By choosing a negative potential of -55 V it was possible to stop electrons in their path of travel and by doing so to eliminate the ion generation and FT-ICR signal. But as the voltage was turned to positive values, no increase above the signal already achieved by the solemn operation of the cathode was possible. This is in contradiction to the work mechanism of the ion source where accelerated electrons should have increased ionization probability. This

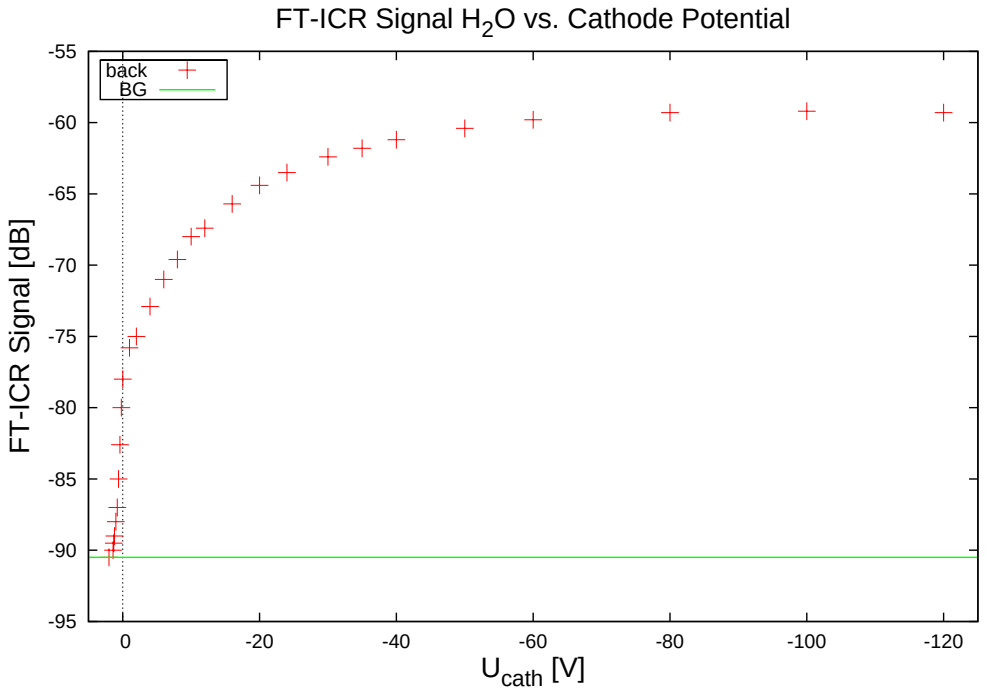

Figure 5.14: **FT-ICR signal as function of the applied cathode voltage.** [$U = (var, 0, 0, 0); p = 10^{-7}$mbar] Plotted is the signal as elevation over the background.

was the first hint that the ions detected at the FT-ICR were not generated at the region of the ion source. The variation of the cylinder and extractor voltage confirmed this assumption. According to the work mechanism, positive and negative voltages applied there should increase the number of ions. Such an effect on the signal could not be seen however.
This can be explained by the strong magnetic gradient any particle must overcome in order to reach the FT-ICR trap. It is situated at a two hundred times higher field. Particles become subject to magnetic mirroring reflecting them back. For uncollided forward directed electrons it is easier to overcome this barrier than it is for isotropically distributed ions which result from collisions.
So is it most likely that ions created by the source are rejected by the magnetic mirror. Forward emitted electrons however overcome this magnetic mirror in large numbers and cause ionization processes in the homogeneous magnetic field. Thereby they created ions which in turngenerate the detected signal at the FT-ICR trap.

Due to this effects this configuration was not feasible for any further characterization measurements. Nevertheless it has proven the proper operation of the photocathode and the FT-ICR trap.

5.4.3.2 Photocurrent

The ion source setup was modified by the so called endplate behind the last electrode, which was mounted to the front side of the vacuum tube. At this position the magnetic field is significantly higher but also has a strong gradient at the position of the electrode system. It rises from 0.9 T at the cathode to 3 T at the extractor position. This magnetic gradient has a great influence on the operation of the ion source: The flux tube of electrons, generated at the photocathode, narrows down along the electrode system, which means a smaller gas volume is enclosed by it. Also the covered cross-section area by electrons and ions narrows down along the beam axis. Possible magnetic mirroring is also the case here starting already within the ion creation region.

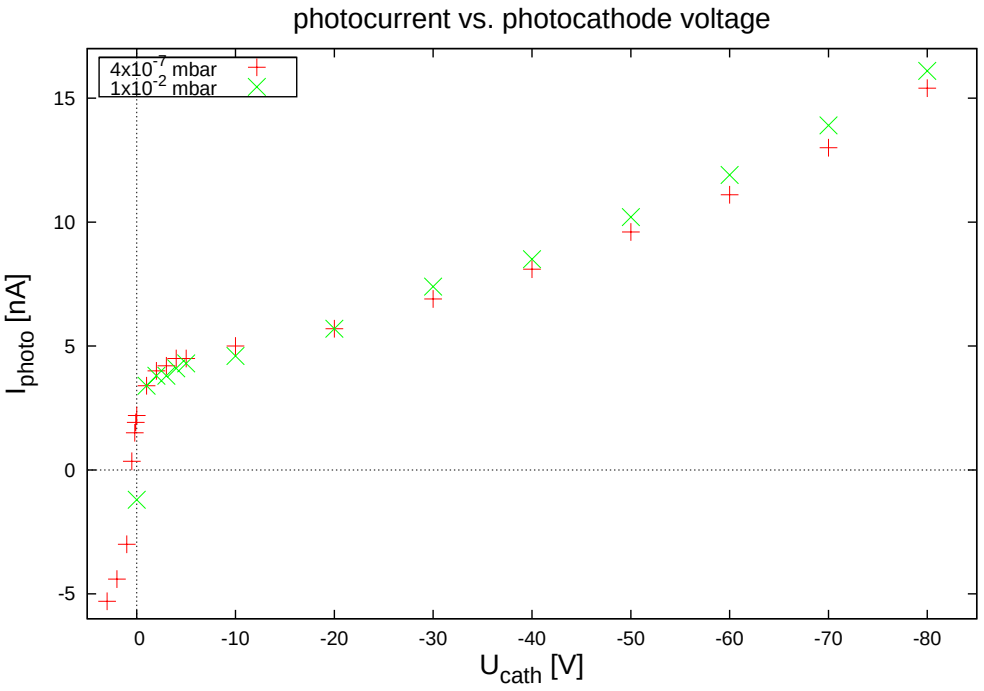

Figure 5.15: **Photocurrent as function of the applied cathode voltage for two different pressures.** [U =(var,0,0,0),$p = (4 \cdot 10^{-7}, 1 \cdot 10^{-2}$ mbar N_2]

Recordings of the photocurrent at the cathode window were taken at the pressures of $4 \cdot 10^{-7}$ and $2 \cdot 10^{-2}$ mbar. The data are plotted in diagram 5.15.
The curves of both pressures lie very close to each other, as it is expected because the pressure does not play a key role in the photoelectrical effect. One observes that the behavior for applied voltages above 0 V until 10 V resembles the expected behavior of a photocathode as it is described in the preceding section. However, the current does not go into saturation if the voltage is increased, but continuously rises further. This can be explained by the magnetic mirroring effect: Agitated electrons are already pushed back to the photocathode if they try to leave with too less longitudinal momentum. These

electrons have indeed participated in the photoelectrical effect, but do not count in the recorded total current at the photocathode. When the voltage at the cathode plane is but increased, the supposed slow photoelectrons receive additional momentum in longitudinal forward direction by electrostatic repulsion. This enables them to overcome the magnetic mirror which was inpentratable for them before the voltage increase. An additional positive accelerator voltage also has a likewise positive effect.
The recorded photocurrents in the region between -10 and $-80\,\mathrm{V}$ cathode voltage have increasing values from 5 nA lowest up to 16 nA. A value of $-50\,\mathrm{V}$ (corresponding 10 nA) was picked again as standard operation voltage for the cathode, as it already had proven as a good refference point in the preceding measurement.

An interesting property in this regard is the quantum efficiency of the photocathode. By the 6 fold increase of the photocurrent as a result of the prevacuum chamber (compare 5.4.2.4) in combination with the emittance spectrum of the UV-lamp (provided by the company) as well as the 190 nm cut-off by air, it was possible to roughly estimate the effective quantum efficiency. The assumption is that all photons participate equally in the photo effect without regard to their energy as long as their energy is well above the work function.
The interesting region of UV-light that agitates electrons in the photocathode is between 150 nm and 210 nm. The lower limit is derived from the transmittance function of the silica vacuum window that cuts off photons below 150 nm wavelength. The upper limit is derived from the cut-off by air in the prevacuum chamber. It accounts for 5/6 of the total photon flux when terminated by pumping. The integral over the number of photons above the cut of 190 nm must thereby account for the rest of 1/6 which is the case when the integral ends at 210 nm.
The total light intensity by all these photons is $12.4\,\mu\mathrm{Wcm}^{-2}$ at a distance of 50 cm. The light spread of the light source is approximately 5°, thus already well illuminating the whole cross-section of the 38 mm diameter cathode window. This corresponds to an effective spot size of $38.9\,\mathrm{cm}^2$ at 50 cm distance or in other terms the loss of 4/10 of the light intensity by bad focusing. The total flux of photons at the cathode but still remains roughly $5.6 \cdot 10^{14}$ photons per second with a mean energy of 7.3 eV.
The highest photocurrents achieved during the measurements at $-50\,\mathrm{V}$ cathode voltage were approximately 10 nA or $6 \cdot 10^9$ electrons per second.
The quantum efficiency is defined as the ration between the number of incident photons and the number of generated photoelectrons. In this case it is

$$QE = \frac{\sharp\text{electrons}}{\sharp\text{photons}} \approx 1 \cdot 10^{-5}$$

In the literature [Jia98] quantum efficiencies for gold of up to 10^{-4} are stated. But those have been achieved by more intensive light sources and better focusing.

5.4.3.3 Electron current

In these measurements the generated electron currents at the endplate were recorded and compared to the initial photocurrent. This should provide additional information about the efficiency of the photon-electron conversion and on how well the electrons

can travel along the magnetic gradient to the extractor electrode.

Diagram 5.16 shows the result of the photocurrent measurement as well as the cur-

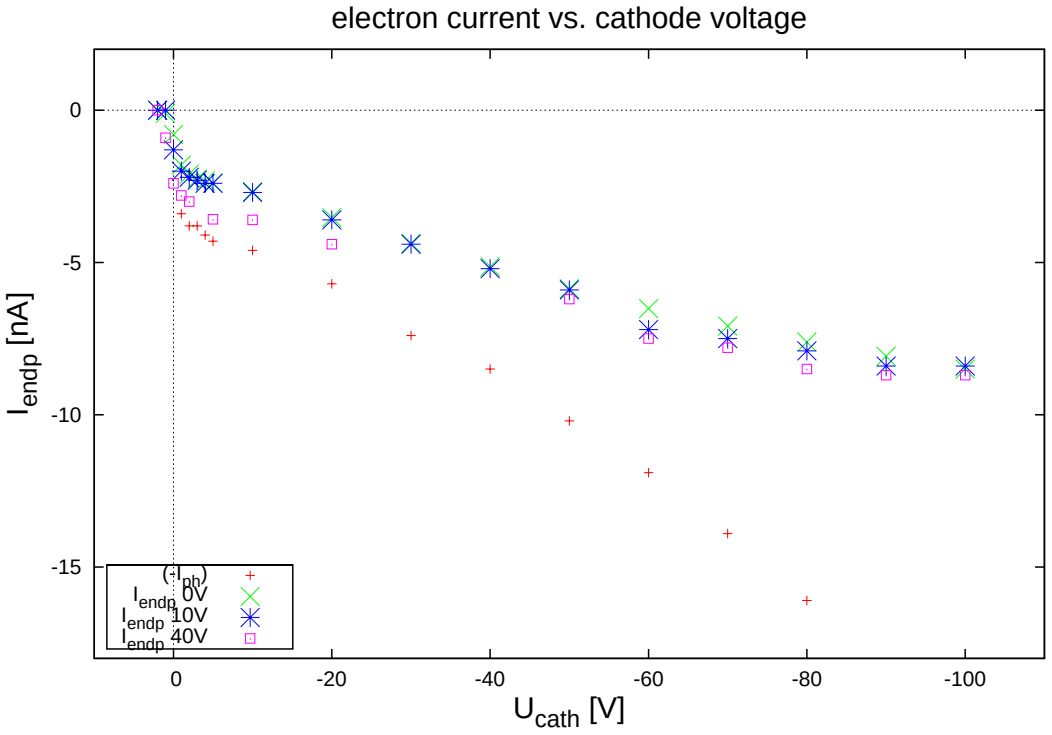

Figure 5.16: **Current at the endplate in function of the applied cathode voltage for 0 V, +10 V and +40 V at the endplate.** [$U = (-50, 0, 0, 0, var); p = 10^{-2}$ mbar air]. The negative values of the currents of at the endplate are plotted as positive for better comparison to the photocurrent plotted also.

rents at the endplate for voltages of 0 V, +10 V and +40 V applied there. These positive voltage configurations are interesting to investigate if anFwhich was attractive potential at the endplate can help the electrons to get there. A change to the value of the neutral configuration was not found. One can then determine which fraction of the photoelectrons actually reaches the endplate. This was found to be only 50 to 60%. Possible removing mechanisms are migration, neutralization or loss by collisions with residual gas atoms. The greatest effect however involves the mirroring of electrons at the magnetic gradient.

Figure 5.17 shows the recorded electron current as a function of the cathode voltage at various pressures of nitrogen. The currents for all three pressures nicely follow the saturation behavior already discussed. The curve for readings at the 10^{-3} mbar level, however, begins to separate from the others curves around 20 V elevating the signal

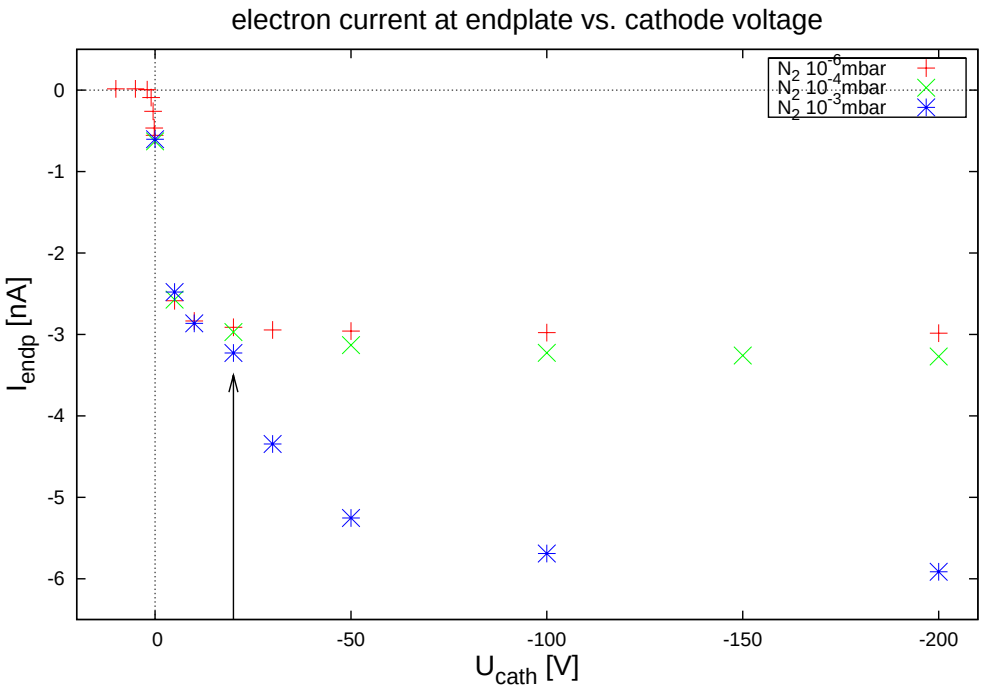

Figure 5.17: **Current at the endplate in function of the applied cathode voltage for different pressures.** $[U = (var, 0, 0, 0, 0); p = (4 \cdot 10^{-6}, 10^{-3}, 10^{-4})\,\text{mbar}\ \text{N}_2)$. Indicated by the arrow is the position where the function for 10^{-3} mbar separates from the other two.

roughly by a factor of 2 above the other curves. An explanation is that at 10^{-3} mbar the nitrogen gas density suffices to cause ionization in large numbers. This is supported by the evaluation of ELIOTT (1) where a plateau of a maximal deuterium ion current was found at $3 \cdot 10^{-3}$ mbar. Ionization effects however not take place until the primary electrons have a sufficient energy, as stated in [IonOL]. This threshold is taken at 16 V and generates an increasing amount of secondary electrons. At higher voltages of 100 and 200 V approximately, one secondary electron is generated per incident primary electron.

5.4.3.4 Ion current

Measurements regarding the ion current were performed to gain more information about the optimum running parameters. The modification of the ion source at the endplate offers the opportunity to measure the ion current directly at the place of its creation without any loss along the beam tube (how it was the case at the ELIOTT (1) setup).

The optimum cathode voltage of -50 V has already been determined by the preceding measurements. As a next step an optimal extractor voltage had to be found in order

to stop and reflect the photoelectrons to purify the ion plasma. To fulfill this task the applied voltage at the extractor electrode must slightly exceed the cathode voltage. In fact the electron current could completely suppressed when a voltage of $-52\,\mathrm{V}$ was applied. To keep a certain safety margin a standard parameter value was fixed to $-55\,\mathrm{V}$.

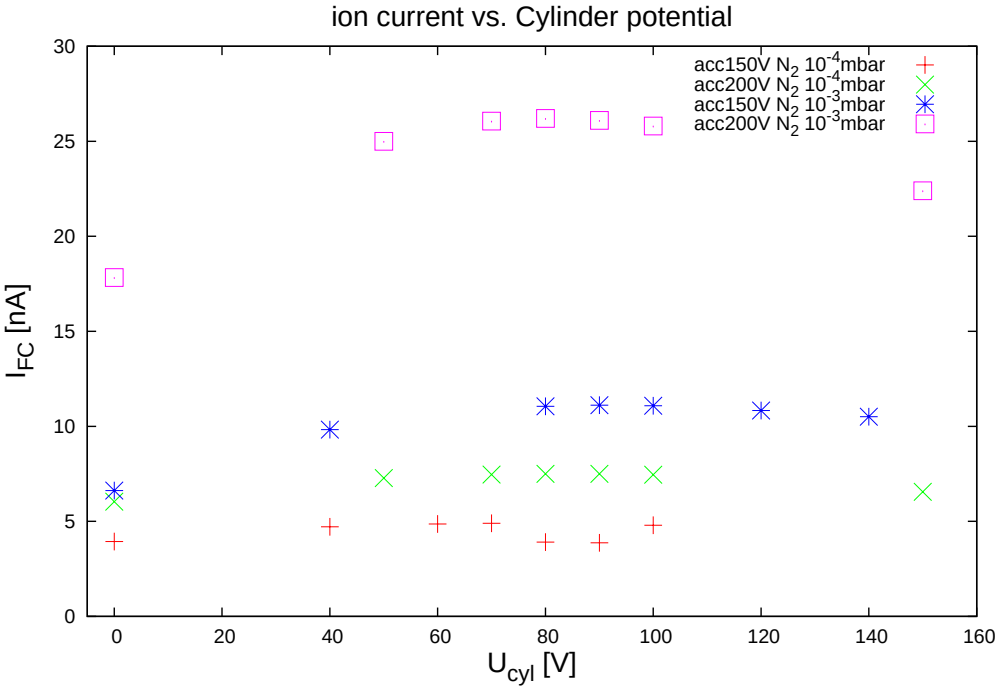

Figure 5.18: **Current at the endplate in function of the applied cylinder voltage.** $[U = (50, (100, 150), var, 0, 0);\ p = (10^{-3}, 10^{-4})\,\mathrm{mbar\ N_2}]$

To finally commission the ion production as intended in the work principle, the accelerator and cylinder potentials must be choosen accordingly. A preferrably high ion current is one goal.
For this the accelerator voltage was varied between +50 and +200 V with a simultaneous variation of the cylinder voltage $[U = (-50, var(+50 \cdots +200), var(0 \ldots acc), -55)]$. For nitrogen pressures of $1.3 \cdot 10^{-4}$ and $1.4 \cdot 10^{-3}$ mbar the peak value of the obtained ion current at the endplate was investigated. For accelerator voltages of +100 V, +150 V and +200 V, and a cylinder voltage of +80 V to +100 V the best results were obtained. **This yielded an ion current of 26.2 nA at a pressure of 10^{-3} mbar nitrogen and applied voltages of -50,+200,+80,-55 at the electrode setup**. This is also the highest value of a pure ion current achieved at the experiment.

When investigating the specific setting of +200 V at the accelerator, the ion current tended to rise slowly, which points to the possible creation and ignition of a Penning trap inside the electrode system. Although this increases the effective number of created

ions it is not a desired mode of operation. It might lead to damage at the electrodes and especially the cathode window through sputtering processes. That is why this mode of operation must be prevented at all circumstances and the operation at such high voltages and pressures must be avoided.

5.4.4 Conclusion

The first measurements with the new ion source ELIOTT 2 have been a success and the concept is very promising for future developments:
The new ion source has proven to be that it was able to produce ions by the intended production mechanism. The operation together with the FT-ICR succeeded.
With the standard operation parameters for the electrode setup U =(-50 V, 150 V, 80 V, -55 V) the ion source can be operated safely in the conditions of the setup. The highest ion current the source was able to provide was 26 nA, even when operating in a magnetic gradient.

The newly developed cathode window showed a quite reasonable quantum efficiency of 10^{-5} for the UV-light for the Hamamatsu light source. This is a result one order of magnitude lower than the findings of [Jia98] which also investigated the properties of thin gold layers for electron emission applications. Their research however is based on the utilization of lasers, which promise a high photocurrent by high radiation intensity but are limited to a very narrow spot size.

Unfortunately, it was not possible to operate the ion source in the homogeneous magnetic conditions it was intended for. At the rear mounting position the magnetic field was far too low to allow created ions from the source to overcome the magnetic mirror of the 250 times stronger field at the center of the magnet.
On the other side of the vacuum tube the ion source had to operate in a strong magnetic gradient, which was the cause of distortions in the ion creation mechanism. Also there were hints of filling and ignition of a Penning trap by operation at this place.

Nevertheless, the obtained data and operation experiences gained by handling the ion source pave the way for improvements such as the extension of the setup (see 5.3.6) for reaching deeper into the magnetic field.
A second set of measurements with the manufactured extension was carried out in May 2009. The electrode setup stood by then was placed in a much more homogeneous field (see table 5.2). Unfortunately, the measurement was shadowed by a strong decrease of UV-light intensity; as the light source had reached its lifespan (500h)[HamLS] and was damaged later during handling. A suitable replacement had to be found, before the calibration measurements with the extended setup could continue.

5.5 Alternative UV light source

While the Hamamatsu light source was unable to operate, a search for a suitable replacement was conducted.

Table 5.2: **Axial magnet field at IS in the extended configuration inserted by front (f)**; additional adapter flange thickness 25 mm

part	pos [cm]	magn.f.(f) [T]
cath	34.3	4.65
acc	35.5	4.69
start cyl	37.5	4.71
end cyl	42.5	4.72
ext	44.5	4.72

An alternative source must necessarily radiate in the far UV regime below the work function of gold ($W_{\mathrm{Au}} = 4.75\,\mathrm{eV} \cong 263\,\mathrm{nm}$). This value might be increased by aging and surface contamination by 0.2 to 0.3 eV ($W_{\mathrm{Au\text{-}cont}} = 5.1\,\mathrm{eV} \cong 244\,\mathrm{nm}$), as stated in [Jia98]. A possible new source must also provide this safety margin. It should also irradiate the photocathode with an intensity comparable to the present light source does ($500\,\mu\mathrm{W}$). This means that the emission characteristics must either be narrowly directed in forward direction to allow a distant mounting on the prevacuum tube, or the light source must be able to operate in a high magnetic field by being small enough to fit inside the prevacuum tube. The latter is very advantageous because the light source thereby can be positioned closely to the cathode window. Losses by bad focusing are minimized and pumping of the prevacuum becomes obsolete.
Investigations for a replacement with outside mounting other than the Hamamatsu model were without result. Either the devices did not fulfill the requirements or the source did not posses a mounting flange to enable pumping.
For the mounting inside the vacuum tube the newly available (V)UV-LED diodes on the market seemed very feasible. For example the model *T9H25C* of Seoul semiconductors provides up to $120\,\mu\mathrm{W}$ radiation power at a peak wavelength of 255 nm (active Au-photo layer) [Seo06]. The advantage of these diodes is that they are very cheap and can be packed in bundles onto a circuit plate to form a high-luminosity light source.
One of these diodes was available to perform a quick check, if the use of this model is feasible. The single diode was however not able to generate a detectable photocurrent in the cathode window of ELIOTT 2. This was partly expected, as the peak wavelength is not in the margin specified above.
Nevertheless this LED option should be closely monitored as the technology advances in the field of semiconductors is quite rapid and LEDs at shorter wavelength might be available in the nearer future.
In the meanwhile a new UV-light source from Hamamatsu of the same model as the old one (L10366) was ordered and is expected to arrive at the end of July so that the measurements with the extended setup can continue.

5.6 Outlook for future and next generation ion sources

The first future task is to resume testing of the extended ion source. The information gained on the performance in strong homogeneous fields motivates new improvements

can be motivated that enhance the overall efficiency of ELIOTT 2.

In the meantime the development of a next generation ion source for the upcoming plasma test experiments with the DPS2-F cryostatcontinues. The concept and innovations of the ELIOTT 2 ion source can be used to guide the design of the new setup. Additional challenges here are:

- the smaller tubing of the DPS, where the beam line at the point of the homogeneous region is only 86 mm wide
- the increased magnetic field strength of 5.6 T
- changes to the design so that a rest light transmittance through the cathode window might not influence other devices (angled setup prohibiting line of sight)

During the present work it was realized that the setup of ELIOTT 2 might already fulfill the demands of such an ion source: minor modifications to the front electrode system would make it able to fit into the beam tube. An adapter flange would solve the mismatching flange sizes. The ELIOTT 2 setup is also in compliance with the vacuum cleanness requirements.

The simulation code of Ferenc Glück is also currently under reconstruction. The results of proper simulations of the ELIOTT ion sources are expected in the nearer future. This will help to better understand how different running parameters influence the ion creation in detail and where possible improvements to the setup can be done. The decision if a new source should be constructed or if the existing setup should be modified but depends on the performance of ELIOTT 2 in future measurements. The results of these studies might reveal necessary changes that in the final choice might prefer the building of a new source.

A publication on the condensed work on the subject of electron impact ion sources is currently in preparation.

6. Summary and conclusion

The search for the neutrino mass remains an open endeavor in general physics and is a handled as major testing parameter for different particle models. It is an important input parameter for particle physics and cosmology. While experiments with different approaches try to measure the neutrino mass, it was until now only possible to set upper limits. Favored by the most theoretical models is a neutrino mass in the sub-eV scale.

The goal of the KATRIN experiment is to determine the neutrino mass by a model-independent approach utilizing the beta-decay of tritium. By carefully measuring the endpoint spectrum of the decay electrons and after 3 years of data-taking KATRIN aims for a sensitivity to the neutrino mass of 0.2 eV. The necessary setup is very complex, as the measurement with such a precision sets high demands.

One key task for the success of the experiment is the removal of radioactive tritium molecules along the beam line. This is accomplished, amongst others, by the DPS2-F, which removes neutral gases by pumping and charged ions by inserted dipole elements. Like all modules the DPS2-F must be tested, if the ready assembled module can truly fulfill the demands of the KATRIN setup. This is accomplished during acceptance and test measurements which validate DPS2-F's properties in gas and ion removal, magnet operation and electron guiding.
The subjects of this thesis evolved around two of those measurements, in peculiar the reduction-factor measurement and the investigation of plasma properties by an ion source.

In the framework of preparations for tests of the ion behavior in the DPS2-F element, and in preparation for tests of ion-removal and detection systems, an ion source for operation in magnetic fields of several Tesla and pressures of 10^{-4} to 10^{-3} mbar was built and optimized. In order to test and characterize it, measurements were performed at a test setup provided by MPI-K Heidelberg. This ion source is based on a back-lit photocathode with a gold overlay on quartz substrate and in a vacuum electrode system. Ion currents of up to 26 nA were measured, which satisfies the requirements of the planned test experiment.

During this thesis contributions to preparations for reduction-factor measurements were accomplished. These especially concerned the calibration of sensor devices of the experimental setup: The residual-gas analyzer (Pfeiffer QMS 200) was calibrated to measure

partial pressures of helium, deuterium, neon, nitrogen and argon. Also the cold cathode Penning gauge (Leybold RP27) and flow controller (MKS M200) were calibrated and the intercorrelated properties of the setup were probed.
By these and additional assessments the reduction factor setup is ready for its application at the DPS2-F and will be used to verify the required reduction factor of 10^5.

Now that the cryostat of DPS2-F has arrived at the experimental site (July 2009), the installation and connection of the cryostat to the TLK infrastructure is currently carried out. After this work's conclusion the acceptance and test experiments with the DPS2-F module to which this thesis has contributed, can finally start.

Bibliography

[Arn01] C. Arnaboldi, "Bolometric Bounds on the Antineutrino Mass", Phys. Rev. Lett. 91, 161802 (2003)

[Bon03] J. Bonn, B. Bornschein, L. Bornschein, M. Glugla, O. Kazachenko, "Tritium related parts of KATRIN: Basic Concepts and Key Requirements", KATRIN internal report, 2003

[Bor03] B. Bornschein *et al.*, "Self-charging of quenched condensed tritium films", J. Low Temp. Phys., 131 (2003) 69

[Cow56] C. L. Cowan, Jr., F. Reines, *et al.*, "Detection of the Free Neutrino: A Confirmation", Science 124, 103 (1956)

[Dav94] R. Davis, "A review of the Homestake solar neutrino experiment", Prog. Part. Nucl. Phys.32:13-32, 1994

[Dia08] M. Ubieto-Díaz, D. Rodrígue, S. Stahl, "Status of the FT-ICR test setup", KATRIN internal report, Feb 2009, BSCW

[Dia09] M. Ubieto-Dáza, D. Rodrígue, S. Lukic, Sz. Nagya, S. Stahl, K. Blaum, "A Broad-Band FT-ICR Penning Trap System for KATRIN", Intl. J. Mass Spectroscopy, 2009

[For09] J. A. Formaggio, "A Rear Electron Gun using Penning Traps", talk, 2009, BSCW

[Fra08] F. Fränkle, "Erste Messungen der elektromagnetischen Eiegenschaften des KATRIN Vorspektrometers", diploma thesis

[FZK06] Dr. J. Hoffmann, "KATRIN kommt!", press release, FZK, 2006

[Glu08] F. Glück, privat communication

[Got08] A. Gotsova, Volume calibration for UF test facility, KATRIN internal report, 2008

[Got09] A. Gotsova, doctoral thesis, in preparation

[Gru09] C. Grupen, B. A. Shwartz, H. Spieler, "Particle detectors", book, p307, 2009

[Ham99] W. Hampel, Gallex collab., "Solar neutrino observations: results for previous termGALLEXnext term IV", Physics Letters B 447.1-2 (1999) p127-133

[HamLS] Hamamatsu, "High brightness VUV light source unit L10366 series", data sheet, `www.hamamatsu.com`

[Han04] S. Hannestad, "Neutrino mass bounds from cosmology", SDU, Nordita, arXiv:hep-ph/0412181v1

[Hoe09] M. Hötzel, "Berechnung von KATRIN Messspektren unter Einbeziehung der Eigenschaften der fensterlosen gasförmigen Tritiumquelle", diploma thesis, 2009

[IonOL] "Online resource for electron impact ionization and excitation data", review, `http://physics.nist.gov/cgi-bin/Ionization/ion_data.php?id=HI&ision=I&initial=&total=Y`
I - BEB Direct
II - BEQ Y.-K. Kim and M.E. Rudd, Phys. Rev. A 50, 3954 (1994).(T)
III - shah87 M. B. Shah, D. S. Elliott, and H. B. Gilbody, J. Phys B 20, 3501 (1987).(E)
IV - gryz65 M. Gryzinski, Phys. Rev. 138, A305, A322, A336 (1965).(T)
V - younger81 S. M. Younger, J. Quant. Spectrosc. Radiat. Transfer 26, 329 (1981).(T)

[Jia98] X. Jiang, C. N. Berglund, and A. E. Bell, "Photoemission from gold thin films for application in multiphotocathode arrays for electron beam lithography", J. Vac. Sci. Technol. B Volume 16, Issue 6, pp. 3374-3379 (1998)

[Kam03] Super-Kamiokande Collaboration, "Solar neutrino measurements in Super-Kamiokande-II", Phys. Rev. D 78.032002 (2008), arXiv:0803.4312

[KDR04] The KATRIN Collaboration, "KATRIN Design Report 2004", FZKA Scientific Report 7090, MS-KP-0501, 2004

[KL03] KamLAND Collaboration, "First results from Kamland; Evidence for reactor anti-neutrino disappearance", Phys. Rev. Lett. 90, 021802 (2003)

[KL04] KamLAND Collaboration, "A high sensitivity search for anti-neutrinos from the sun and other sources at Kamland", Phys.Rev.Lett. 92, 071301 (2004)

[Kla01] H. V. Klapdor-Kleingrothaus *et al.*, "Evidence for Neutrinoless Double Beta Decay", Mod. Phys. Lett. A 16 (2001) p. 2409

[Kla06] H. V. Klapdor-Kleingrothaus and I. V. Krivosheina, "The Evidence for the Observation of $0\nu\beta\beta$ Decay: the Identification of $0\nu\beta\beta$ Events from the Full Spectra", Mod. Phys. Lett. A 21 (2006) p. 1547

[KLI01] A. Osipowic *et al.*, "Letter of Intent", hep-ex/0109033, FZK scientific report 6691, 2001

[Kra04] C. Kraus *et al.*, "Final results from phase II of the Mainz neutrino mass search in tritium beta decay", Eur. Phys. J.C40:447-468,2005

[Lan03] K. Landea, P. Wildenhaina, "The Homestakenext term chlorine solar neutrino experiment-past, present and future", Nuc. Phys. B 118 (2003) p49-54

[Ley02] Laybold Vacuum, "Grundlagen der Vakuumtechnik", book, p137,138

[Lob99] V.M. Lobashev *et al.*, "Direct search for mass of neutrino and anomaly in the tritium beta spectrum", Phys. Lett B460 (1999) 227

[Lob99] V. M. Lobashev *et al*, "Direct search for mass of neutrino and anomaly in the tritium beta-spectrum", Phys. Lett. B 460 (1999) 227

[Lor01] T. J. Loredo, D. Q. Lamb, "Bayesian analysis of neutrinos observed from supernova SN 1987A", Phys. Rev. D 65.063002 (2001)

[Luk08a] S. Lukić, "Gas-Flow Reduction Factor in function of the pumping efficiency of the system connected to the output of DPS2-F"', KATRIN internal report, 2008, BSCW

[Luk08b] S. Lukić, "Report on the design of the photocathode ion source", KATRIN internal report, 2008, BSCW

[Luk08c] S. Lukic, M. Zoll, "Pfeiffer RGA Kurzbetriebsanleitung"-ger, internal short manual, BSCW, 2008
S. Lukić, "'Pfeiffer RGA Short User's Manual"-eng, manual, BSCW, 2008

[Luk09a] S. Lukič *et al*, "Report on test and calibration phase for the gas-flow reduction measurement on DPS2-F for KATRIN", KATRIN internal report, Uni-Ka / FZK, 2008-2009, BSCW

[Luo05] X. Luoa *et al.*, "Monte Carlo simulation of gas flow through the KATRIN DPS2-F differential pumping system", Vacuum 80, Issue 8 (2006) p864-869

[Mau09] D. Maurel, "Beta flux determination with bremsstrahlung x-ray", talk, 2009, BSCW

[Mon09] B. Monreal, "Rear Wall design concepts", talk, 2009, BSCW

[Nak07] K. Nakamura, "solar neutrino review", review, 2007, `http://pdg.ift.unesp.br/2009/reviews/rpp2009-rev-solar-neutrinos.pdf`

[Ott08] E. W. Otten and C. Weinheimer, "Neutrino mass limit from tritium β decay", review, Rep. Prog. Phys. 71 (2008) 086201 (36pp)

[PDG08a] C. Amsler *et al.*, (Particle Data Group), "Neutrino Mixing", review, PL B667, 1 (2008)

[PDG08b] C. Amsler *et al.*, (Particle Data Group), "Neutrino properties", review, PL B667, 1 (2008)

[Pay99] R. Payling, The Spectroscopy Net . Com, Light absorption in air, `http://www.thespectroscopynet.com/Index.html?/Extreme_UV_2.html`

[PfePri] Pfeiffer Vacuum, "QMS 200 Quadrupol-Massenspektrometer Prisma", operation manual, BSCW

[PfeQS] Pfeiffer Vacuum, "Quadstar 32-bit", software documentation, BSCW

[Rei09] S. Reimer, "Elektrostatisches Dipolsystem in der DPS2-F zur Neutralisierung von Ionen im Transportsystem des KATRIN Experimentes", KATRIN internal report, 2009, BSCW

[Rei09] S. Reimer, "Kalibrierung der Kaltkathode RP303 im DPS2-F Testexperiment", KATRIN internal report, Uni-Ka, 2009, BSCW

[Rein56] F. Reines, C. L. Cowan, Jr., "The Neutrino", Nature 178, 446 (1956)

[Schl09] K. Schlösser, S. Lukić, M. Zoll, "Leak detector - summary of preliminary tests", KATRIN internal report, 2009

[Scho08] M. Schöppner, "'A Prototype Ion Source for the Functionality Test of KATRIN Transport Section", diploma thesis, 2008

[Schw09] J. Schwarz, diploma thesis, in preparation

[Seo06] Seoul semiconductors, "T9H25* VUV-LED Specifications", data sheet

[Ver02] V. M. Vermula, "Results from SAGE", Nuclear Physics B - Proceedings Supplements, Volume 110, July 2002, Pages 315-319

[Wei99] C. Weinheimer *et al.*, "High precision measurement of the tritium beta spectrum near its endpoint and upper limit on the neutrino mass", Phys. Lett B460 (1999) 219

[Zol08] M. Zoll, S. Lukić, 'Properties of thin layers of Au for photo electron emission by UV light', Sept 2008, BSCW

[Zol09a] M. Zoll, "'Verification of running properties of ELIOTT 1", KATRIN internal report, Jan 2009, BSCW

[Zol09b] M. Zoll, "Test Measurements of ELIOTT 2 (FT-ICR Test Ion Source)", KATRIN internal report, Feb 2009, BSCW

Acknowledgements

Für meinen Vater

Ich danke all den Leuten, die bei dem erfolgreichen Abschluss dieser Arbeit beteiligt waren.

Zu erwähnen sind in diesem Sinne Guido Drexlin und Beate Bornschein, die die Mittel und die Supportstruktur für diese Arbeit am Projekt KATRIN bereitgestellt haben. Im gleichen Zuge ist auch Strahinja Lukić, meinem anleitenden Betreuer zu danken, der immer mit einer helfenden Hand und Unterstützung aufwarten konnte, auch wenn es um sprachliche Unklarheiten im Englischen ging.

Desweiteren ist hier auch der Gruppe der Werkstatt und allen anderen Helfern Dank geschuldet, die stets prompt alle technischen Schwierigkeiten ausräumen konnten.

Auch der Laborgruppe des MPI-K Heidelberg sei gedankt für Hilfe beim Einbringen und Vermessen der Ionenquelle.

Desweiteren seien hier noch meine Kollegen erwähnt, die das eine Jahr Institutsleben und besonders die Kaffeerunden bereichern konnten.

Ansonsten ist da noch das Gegenteam Slitherin aus dem TLK.

Dank auch an all die Persönlichkeiten, die ich während meiner Studienzeit kennen lernen konnte, derer ich einige meine Freunde nennen darf und deren Liste jedoch viel zu lang wäre sie hier anzubringen.

Ebenfalls meinem sehr stillen Laborkollegen Eddie und all denjenigen, die sich jetzt hier nicht gefunden haben.

Zu guter Letzt bleibt der größte Dank jedoch meiner Familie auszusprechen, die mich die Jahre meines Studiums in vielerlei Hinsicht unterstützt hat:

Heidi, Phoebe und Alexander

Declaration of originality

I hereby declare that the work submitted is my own and that all passages and ideas that are not mine have been fully and properly acknowledged.

Hiermit versichere ich die vorliegende Arbeit selbständig angefertigt, alle dem Wortlaut oder Sinn nach entnommenen Inhalte anderer Werke an den entsprechenden Stellen unter Angabe der Quellen kenntlich gemacht und keine weiteren Hilfsmittel verwendet zu haben.

Marcel Christian Robert Zoll, August 2009